Allelic Variation at 9p21.3 Orchestrates Widespread RNA Splicing Shifts Governing Vascular Smooth Muscle Cell Plasticity

Suryavanshi S.[1#], Yang H. [1#], Salido E. [1] and Lo Sardo V[1]*.

Department of Cell and Regenerative Biology; University of Wisconsin-Madison; Madison, WI 53705, USA

[#] These authors contributed equally

*Corresponding Author:
Dr. Valentina Lo Sardo, PhD
Department of Cell & Regenerative Biology
University of Wisconsin-Madison
School of Medicine and Public Health
Madison, WI 53705
Email: losardo@wisc.edu

ABSTRACT

Genetic risk for coronary artery disease (CAD) has been linked to variants across more than 300 genomic loci. Among them, the 9p21.3 locus has the strongest and most consistent association with CAD, accounting for roughly 13% of cases. Despite its prominence, the mechanisms by which this locus influences vascular cells remain unclear. Here, we applied haplotype-biased genome editing in induced pluripotent stem cells (iPSCs), followed by differentiation into vascular smooth muscle cells (VSMCs), to compare the effects of the risk and non-risk 9p21.3 haplotypes within an identical genomic background. Using long-read RNA sequencing, we identified distinct allele-specific transcriptional programs driven by the two haplotypes. We unravel extensive reprogramming of mRNA splicing across the transcriptome, which leads to VSMC aberrant phenotypic modulation. We show that the 9p21.3 risk haplotype does not merely alter gene expression but also disrupts transcript isoform expression and usage causing VSMCs to transition to a pro-calcification, osteochondrogenic state. This includes the emergence of novel transcripts and aberrant isoform regulation in numerous CAD-related genes. We prioritized DDX5, previously implicated in CAD through GWAS. Modulating DDX5 in VSMCs was sufficient to mitigate the risk-associated cellular phenotype. Together, this work provides the first comprehensive isoform-level transcriptomic comparison of the two major haplotypes at the 9p21.3 locus. It uncovers allele-specific transcriptional programs that reshape alternative splicing in VSMCs and influence their phenotypic plasticity, thereby increasing CAD risk. We propose a 9p21.3-DDX5 axis as a key regulator of VSMC phenotypic modulation and provide a novel resource of targetable transcripts for reducing cardiovascular risk.

INTRODUCTION

Coronary artery disease (CAD) remains a leading cause of death worldwide affecting approximately 20 million people in the United States[1] . Risk for CAD has a significant genetic component, with a heritability estimate of about 40-60%[2–6]. About 25% of the 300+ CAD risk loci identified by genome-wide association studies (GWAS) are predicted to influence vascular function[7,8], underscoring the importance of vascular integrity in CAD pathogenesis. The 9p21.3 locus — a 60 kb region on human chromosome 9 — was the first genetic region linked to increased CAD risk by three independent GWAS[9–11] and remains the most impactful single genetic risk factor identified to date[12,13]. This primate-specific gene desert contains ~80 SNPs in strong linkage disequilibrium across most populations, forming two major haplotypes: a risk haplotype, increasing disease susceptibility, and a protective non-risk haplotype[9–12,14]. The risk haplotype accounts for 10-15% CAD incidence in the US, making 9p21.3 the costliest disease-linked genomic region[15]. The region partially overlaps ANRIL (**Fig S1A**), a long non-coding RNA gene that is extensively spliced[16,17] . Despite its prominence, the mechanism through which the 9p21.3 risk haplotype drives CAD remains poorly understood.

We previously generated induced pluripotent stem cells (iPSCs) from individuals homozygous risk (RR) and non-risk (NN) at 9p21.3 and used haplotype editing to assess the function of this genomic region in cell types majorly affected by CAD[18]. Using iPSC-derived vascular smooth muscle cells (VSMCs), we showed that the risk haplotype induces multiple CAD-relevant phenotypes, including changes in expression of several genes involved in proliferation, adhesion, and contraction, accompanied by the relative functional defects. More recently, employing single-cell transcriptomics, we showed that the risk haplotype causally drives an osteochondrogenic VSMC state characterized by impaired migration and increased calcification — features consistent with disease-prone VSMCs in human atherosclerotic plaques[19] .

To identify regulators that may function upstream and drive the 9p21.3-specific VSMC phenotypic modulation, we further interrogated our datasets and focused on intermediate-effect genes, focusing on transcription and splicing regulators that often exert modest but consequential changes in expression. This analysis revealed a substantial alteration of splicing regulators.

Alternative splicing is increasingly recognized as a central pathogenic mechanism in cardiovascular disease, contributing to heart failure[20,21], atherosclerosis[22–24] , and vascular remodeling[25]. Variants disrupting splicing regulators or splice sites have been implicated in congenital heart disease[26–28], while mis-regulation of key factors such as RBFOX1[20], RBM20[21], SRSF3[29], and CELF1[30] is known to impair cardiac or vascular function. However, less is known about how SNPs within CAD-associated loci affect alternative splicing and how these events may shape cellular identity, state and function.

Here, employing independent isogenic iPSC collections we uncovered a thus-far undescribed alteration of splicing processes in VSMCs carrying the risk haplotype at 9p21.3, compared to knockouts and non-risk VSMCs. We developed a new isogenic iPSC model enabling precise comparison of the risk and non-risk 9p21.3 haplotypes within an identical genetic background and used long-read sequencing (PacBio IsoSeq) to accurately quantify transcript isoforms. We discovered that the risk 9p21.3 haplotype profoundly rewire gene expression, isoform abundance, and isoform usage genome-wide in iPSC-derived VSMCs. These changes shift cells toward an osteochondrogenic, disease-prone state with reduced vascular remodeling capacity. Importantly, the two haplotypes at 9p21.3 (risk and non-risk) differentially regulate numerous novel transcripts and alter isoform expression and usage of genes previously implicated in CAD.

Among these, we identified DEAD-box helicase 5 (DDX5) — an RNA helicase linked to CAD risk through GWAS[31] — as a key effector of the 9p21.3 regulatory program. Previously shown to be implicated in heart failure, DDX5 has been recently described in VSMC functionality[32]. In our system, DDX5 exhibits distinct isoform profiles depending on 9p21.3 haplotypes. Using CRISPRi to reduce the aberrant DDX5 expression in risk-haplotype VSMCs, we were able to mitigate the osteochondrogenic phenotypes.

Together, our findings reveal a central role for the 9p21.3 locus in reshaping the alternative-splicing landscape of VSMCs and driving their transition into a pathogenic state. Our findings uncover a mechanistic link between 9p21.3, DDX5 and splicing regulation, offering new insights into how this major

genetic risk factor promotes CAD and inform on new therapeutic targets to correct splicing imbalance in vascular disease.

RESULTS

RNA sequencing predicts splicing alterations in VSMCs driven by the 9p21.3 risk locus

We previously achieved complete deletion of the human 9p21.3 coronary artery disease (CAD) risk locus in induced pluripotent stem cells (iPSCs) derived from both risk and non-risk genetic backgrounds[18]. Using iPSCs generated from one homozygous risk donor and one homozygous non-risk donor, we successfully excised the entire ~60 kb haplotype. Following this deletion, we established an isogenic panel of iPSCs comprising four genotypes: RR (both risk haplotypes intact), RRKO (isogenic risk knockout; homozygous deletion of both risk alleles), NN (both non-risk haplotypes intact), and NNKO (isogenic non-risk knockout; homozygous deletion of both non-risk alleles). Terminally differentiated iPSC-derived VSMCs were collected for bulk RNA sequencing and differential expression analysis. We previously characterized a major transcriptional signature unique to RR VSMCs relative to the other three genotypes (RRKO, NN, NNKO). Differentially expressed genes showing high fold changes, mapped to key VSMC functions such as proliferation, adhesion, and contractility[18]. Our prior work focused on genes displaying large expression changes (> absolute 1.5 $\log_2$ fold change), however, transcriptional regulators frequently exhibit modest yet functionally consequential changes in expression. Hence, we sought to extend our investigation to encompass genes with moderate but potentially regulatory shifts (< absolute 1 $\log_2$ fold change). Gene Ontology (GO) enrichment analysis using ClusterProfiler on 4,155 genes (**Fig. 1A-B**), revealed significant overrepresentation of pathways associated with RNA splicing (GO:0008380, GO:0000375, GO:0000398, GO:0000377, GO:0000381, GO:0043484, GO:0048024) and mRNA processing (GO:0050684) among the genes upregulated in RR VSMCs relative to all other genotypes (**Fig. 1B**, **Table S1A**). In contrast, pathways associated with ER and Golgi transport (GO:0048193, GO:0006888) were enriched in the non-risk and knockout lines (**Fig. S1B, Table S1B**). These findings suggest that aberrant RNA splicing may constitute a core molecular phenotype driven by the 9p21.3 CAD risk haplotype.

Remarkably, of the 477 genes associated with RNA metabolism and splicing processes in the gene ontology database, 149 genes were upregulated in RR VSMCs relative to both non-risk and knockout lines (**Fig. 1C, S1C**). Several of these genes (e.g., RBFOX1[20] , RBM20[21] , SRSF3[29]) have established links to cardiovascular disease, while some have not been described in connection to CAD (e.g., NOVA1, PTBP2, KHDBRS2), suggesting that this locus may influence splicing regulation beyond its immediate genomic region. Importantly, none have previously been associated with the 9p21.3 risk haplotype.

Functional categorization of the 149-gene set revealed that the majority (31.76%) encode canonical RNA splicing factors. The remainder include regulatory proteins (21.62% transcription factors, kinases, protein modifying enzymes), RNA metabolism factors (14.19%), RNA processing factors (6.08%), RNA helicases (5.41%) (**Fig. 1D**). This distribution indicates that splicing dysregulation in 9p21.3 CAD risk VSMCs

encompasses a broad repertoire of RNA metabolism proteins extending beyond the core spliceosome machinery. Collectively, these analyses reveal a transcriptional enrichment for RNA splicing–related genes in 9p21.3 RR VSMCs, suggesting that disrupted splicing regulation represents a key molecular signature of the 9p21.3 CAD risk haplotype.

Establishing a system to compare 9p21.3 haplotype-specific contributions in VSMCs

To further characterize how the 9p21.3 risk and non-risk haplotypes contribute to splicing-associated gene dysregulation and to evaluate potential transcriptome-wide splicing alterations, we generated a new collection of isogenic iPSC lines using our previously established and validated genome editing strategy for the 9p21.3 CAD locus[18]. Starting with iPSC from a heterozygous individual (carrying one copy of the risk and one copy of the non-risk haplotype at 9p21.3), we performed targeted haplotype deletion. This approach enabled us to establish an isogenic collection including hemizygous clones retaining either the risk (R/KO or R) or non-risk (N/KO or N) allele at 9p21.3 (**Fig. 1E**). These isogenic lines allow precise dissection of haplotype-specific effects within an otherwise identical genetic background. Genotypes were confirmed by PCR (**Fig. S1D**) and validated by Sanger sequencing of SNPs rs1333049 and rs1057278, located within the 60 Kb CAD-associated region (**Fig. S1E**). Immunostaining for the pluripotency marker NANOG demonstrated that all newly generated isogenic lines retained pluripotency (**Fig. S1F**). Lines carrying only the risk allele (R), only the non-risk allele (N), or both alleles (Het) were then differentiated into VSMCs. Successful differentiation was verified by immunostaining for the canonical VSMC markers calponin (CNN1) and transgelin (TAGLN), with all lines reaching full differentiation by day 17 (**Fig. 1F**). We previously showed that VSMCs homozygous for the risk haplotype (RR) express significantly higher levels of short ANRIL transcripts (ending in exon 13) compared with homozygous non-risk VSMCs (NN), while the long ANRIL isoforms (ending in exon 20) do not exhibit genotype-specific differences[18,19]. We also demonstrated that the risk haplotype drives upregulation of osteochondrogenic markers such as SOX9, COL2A1, and CYTL1[19].

Consistent with these prior results, qPCR analysis of VSMCs differentiated from the new isogenic lines (R, N, and Het) revealed a significant upregulation of short ANRIL isoforms in R VSMCs compared with both N ($p<0.0001$) and Het controls ($p<0.0001$), while long ANRIL expression did not differ between R and N (**Fig. 1G**). Similarly, expression of the osteochondrogenic markers SOX9 and COL2A1 was significantly higher in R cells relative to N (SOX9 $p=0.0002$; COL2A1 $p=0.0001$) and Het cells (SOX9 $p=0.0079$; COL2A1 $p=0.0112$) (**Fig. 1H**). Finally, we assessed splicing-related genes identified in our earlier analyses and confirmed that R VSMCs maintain elevated expression of NOVA1 ($p<0.0001$) and PTBP2 ($p<0.0001$) compared to N VSMCs (**Fig 1I**). Together, these results demonstrate that our new isogenic line collection robustly recapitulates our previous findings using an independent donor background. Moreover, these data indicate that the risk allele exerts a dominant effect; a single copy of the 9p21.3 risk haplotype is sufficient

to reproduce the upregulation of short ANRIL isoforms, osteochondrogenic markers SOX9 and COL2A1, and the splicing-related genes previously observed in RR VSMCs.

9p21.3 allele-specific gene expression signature in VSMCs

To evaluate the contribution of the 9p21.3 risk and non-risk haplotypes to genome-wide splicing regulation, we employed PacBio long-read RNA sequencing and profiled gene and transcript expression in isogenic VSMCs carrying distinct genotypes at the 9p21.3 CAD locus. R, N, and Het isogenic libraries achieved high-quality annotation (**Fig S2A**), with 72.1% of reads categorized as full splice matches (FSM), 15.7% as incomplete splice matches (ISM), 5.9% as novel in catalog (NIC), and 5.6% as novel not in catalog (NNIC) (**Fig S2B**). All samples showed comparable proportions across transcript classes (FSM, ISM, NIC, NNIC) (**Fig S2C**).

Differential gene expression (DEG) analyses were performed across three pairwise comparisons: N vs R; N vs Het; R vs Het. The N vs R comparison yielded 656 DEGs ($p < 0.05$), including 268 upregulated and 388 downregulated in R VSMCs (**Fig 1J**). The N vs Het comparison identified a total of 1324 DEGs ($p < 0.05$), with 645 genes upregulated and 679 downregulated in Het VSMCs compared to N VSMCs (**Fig S2D**). Conversely, R vs Het showed only minimal transcriptional differences, with 9 DEGs in total, indicating a highly convergent transcriptional signature (**Fig 1J**). Notably, the comparisons N vs R and N vs Het shared 495 common DEGs perturbed in the presence of the risk allele, indicating a dominant effect of the 9p21.3 risk haplotype exerting a strong transcriptional influence even in the heterozygous state (**Fig S2E**). Gene Ontology (GO) enrichment analysis of DEGs from N vs R and N vs Het revealed strikingly similar biological signatures, concordant with our previous studies on an independent isogenic line collection[18,19]. Genes downregulated in R VSMCs were enriched for processes involved in vascular development, wound healing, and smooth muscle maintenance (e.g., circulatory system development, cell adhesion, migration and muscle development) (**Fig 1K**). Interestingly, one of the top genes downregulated in R and Het VSMCs was APELA/ELABELA (**Fig 1J, S2D**), an endogenous ligand of the Apelin receptor, strongly implicated in heart development[33] and particularly in promoting coronary vessel sprouting[34,35]. This suggests that the 9p21.3 haplotype may play a key role in coronary vessel maintenance, vascular remodeling, and angiogenesis — processes that may be compromised by the presence of the risk allele.

In contrast, genes upregulated in R VSMCs were predominantly associated with skeletal development, osteoblast differentiation, Wnt signaling pathway and cell division (**Fig 1K**). The N vs Het comparison largely mirrored these trends with genes upregulated in Het cells enriched for osteoblast differentiation, (**Fig 1K**).

Together, these data reinforce our earlier results showing that the 9p21.3 risk haplotype strongly influences pathways governing osteochondrogenic state acquisition in VSMCs. Importantly, we show that this effect on cell state is independent of genetic background. The presence of the risk allele at 9p21.3, either in hemizygosity or heterozygosity, is sufficient to drive VSMCs toward an osteochondrogenic phenotype.

Within the same genetic background, selective loss of either the non-risk or risk haplotype shifts the global transcriptomic landscape toward distinct differentiation trajectories — vascular versus osteogenic — highlighting a pivotal role for 9p21.3 in fate determination, potentially through alternative splicing reprogramming.

Haplotype-dependent regulation of transcript isoforms shapes VSMC cell state

Long-read sequencing technology enables the detection of fine-grained transcriptomic differences that are often undetectable using short-read approaches. Leveraging PacBio long-read RNA sequencing in isogenic VSMCs carrying distinct haplotypes, we systematically surveyed transcripts differentially expressed as a consequence of the 9p21.3 genotype. Using the same three pairwise comparisons described above, we identified thousands of transcripts exhibiting allele-dependent expression differences. In the N vs R comparison, 754 transcripts were upregulated and 751 downregulated in R. The N vs Het comparison revealed 775 transcripts upregulated and 579 downregulated in Het versus N VSMCs (**Fig 2A**). A strong overlap of 734 transcripts was detected between the N vs R and N vs Het comparison (**Fig S2F**). Although the R vs Het comparison showed only a modest number of differentially expressed genes at the gene level (n = 9), long-read sequencing detected 58 differentially expressed transcripts between these two genotypes, underscoring the enhanced sensitivity of full-length transcriptome profiling to subtle expression changes (**Fig 2A**).

Transcripts differentially expressed in N vs R represented 1268 unique genes. Approximately 71% of these genes were consistently altered in the N vs Het comparison, indicating a high degree of transcriptional similarity between R and Het VSMCs.

Unsupervised clustering of transcripts based on expression patterns revealed five major clusters: Cluster I - *transcripts upregulated primarily in Het and R cells*, enriched for regulation of cell differentiation and RNA metabolic processes. Cluster II - a shared signature of *transcripts modestly upregulated in both R and Het cells* compared with N VSMCs, enriched for cell cycle regulation and cytoskeletal organization. Cluster III - *transcripts uniquely upregulated in R cells*, associated with skeletal development, neuronal projection, and Notch signaling. Cluster IV - *transcripts upregulated in N VSMCs*, modestly retained in Het cells and absent in R cells enriched for proliferation and circulatory system development. Cluster V - *a signature exclusive to N cells*—absent in those carrying the risk allele—linked to tube morphogenesis, blood vessel formation and development, and vascular structure organization (**Fig 2B**).

To identify potential genomic hotspots, we mapped the chromosomal distribution of differentially expressed transcripts across all comparisons. Both N vs R and N vs Het exhibited broadly distributed allele-specific transcriptional changes throughout the genome (**Fig 2C and S2H**). Remarkably, normalizing transcript counts by chromosomal length revealed enrichment (as a ratio >0.5) of upregulated transcripts on chromosomes 17 and 19, and enrichment of downregulated transcripts on chromosome 20 (**Fig 2C and S2H**). In contrast, the 58 transcripts resulted from the R vs Het comparison did not show any significant

chromosomal enrichment. Importantly, consistent with our prior findings, no enrichment of differentially expressed transcripts was detected on chromosome 9, supporting the model that the 9p21.3 locus acts primarily in trans rather than through local cis-regulatory mechanisms (**Fig 2C)**.

PacBio long-read sequencing also enabled the discovery of hundreds of novel transcripts, categorized as novel in catalog (NIC) and novel not in catalog (NNIC). These correspond to previously unannotated isoforms of known genes, arising either from new combinations of annotated exons (NIC) or from junction of novel exons (NNIC). In total, we identified 268 novel transcripts differentially expressed ($p<0.05$), accounting for 248 unique genes, in R cells compared with N cells (**Fig 2D**). A total of 382 novel transcripts, accounting for 331 genes, in Het cells compared with N, with 141 overlapping between these two comparisons (**Fig S2I**). Gene ontology (GO) analysis of these novel transcripts revealed enrichment in biological pathways primarily related to regulation of cell differentiation. These transcripts represent previously uncharacterized splicing events and novel mRNA isoforms in VSMCs, potentially influencing cell state transitions and associated cellular functions, warranting further investigation.

9p21.3-driven splicing alterations extend to other CAD genomic loci

We previously showed that the risk haplotype at 9p21.3 drives differential expression of multiple genes within other CAD-associated genomic loci in iPSC-VSMCs (i.e. ZEB2, PDGFD, COL4A1, COL4A2, PROCR)[18,19]. Using the most recent meta-analysis of CAD loci by Kessler and colleagues[8] , we examined 198 genes predicted to be causal within established CAD genomic regions. Remarkably, we identified 32 transcripts that were differentially expressed in the N vs R comparison and 37 transcripts in the N vs Het comparison (**Fig 2E, S2J**). We confirmed changes in gene expression that we have previously reported using bulk and scRNAseq (e.g. CXCL12, COL4A1, COL4A2, REST and others) and additionally identified specific known transcript isoforms — as well as previously unannotated transcripts — of CAD genes that are altered by the 9p21.3 risk haplotype. Notably, our novel isogenic system resolved changes in genes that were not detected before. Among the top candidates, we observed differential expression of ANGPTL4, SCARB1, PCSK9, TGFB1, STAG1, MFGE8, FNDC3B, TEX2, CDKN1A in R or Het compared to N VSMCs (**Fig 2F, S2K**). Importantly, transcript-isoform-level analysis revealed additional alterations in isoforms of LDLR, LMOD1, HNRNPUL1, EDNRA, DDX5 (**Fig 2F**). We classified the 198 CAD genes based on their predicted biological functions and roles in atherosclerotic plaque development, following Kessler et al. (**Fig 2F**). We observed an enrichment of transcripts involved in plaque initiation and progression; however, significant changes were present across genes involved in all stages of plaque formation. These findings support a model of 9p21.3 contributing to multiple phases of CAD pathogenesis.

Splicing alteration has minimal impact on chromosome 9 genes

Work from our group and others has shown that the 9p21.3 locus alters the expression of its neighboring genes, CDKN2A and CDKN2B, although substantial variability has been reported, consistent with tissue- and cell type-specific effects[16] .

Here, we sought to investigate local splicing alterations and isoform-switching events affecting genes on chromosome 9. Our initial analyses did not identify a significant enrichment of splicing events on this chromosome, suggesting that the local impact of the 9p21.3 haplotype on splicing is modest. Transcript-level analysis revealed 21 transcripts significantly upregulated in R VSMCs compared to N, including ASPN, IL11RA, PSMD5 and 22 transcripts that were downregulated (**Fig S3A**). In the N vs Het comparison, we observed 29 transcripts upregulated (e.g. TLE, CEMIP2, PSMD5) in Het and 19 downregulated (**Fig S3A**).

Haplotype-specific isoform usage reveals novel target of 9p21.3 in VSMCs

The isoform diversity revealed by long-read sequencing allowed us to identify transcript-level changes that occur independently of alterations in overall gene expression. This approach enabled the detection of differential transcript usage (DTU) even when total gene expression remained comparable across genotypes. Although individual genes can produce multiple transcript isoforms, the relative abundance and usage of these isoforms can profoundly influence cellular function and trigger downstream effects. Our analysis showed that the risk and non-risk haplotypes at the 9p21.3 locus are associated with extensive differential isoform usage, involving 187 transcripts in the N vs R comparison and 91 transcripts in the N vs Het comparison (**Fig S4A**). These correspond to 132 and 66 genes, respectively (**Fig 3A**). In contrast, the R vs Het comparison yielded only two genes exhibiting differential isoform usage, consistent with our previous observation of minimal transcriptional differences between these genotypes (**Fig 3A**).

The N vs R analysis uncovered several cardiovascular-related genes, that were not detected in our previous dataset, including P4HB, DDX5, CALD1, UGP2, SEPTIN9 and LDLR (**Fig S4E-F**). Additionally, 41 genes displayed transcripts that were differentially used in both R and Het cells compared with N VSMCs (**Fig S4B**).

To characterize the splicing events underlying these isoform changes, we categorized alternative splicing events across comparisons, including Alternative Transcription Termination Sites (ATTS), Intron Retention (IR), Exon Skipping (ES), Alternative Transcription Start Sites (ATSS), Multiple Exon Skipping (MES), Alternative 5′ Splice Sites (A5 gain), and Alternative 3′ Splice Sites (A3 gain). Isoforms preferentially used by R VSMCs showed significant increases in ATTS and ATSS events relative to N cells, whereas N VSMCs preferentially utilized isoforms arising from ES, A5, and A3 events. Het cells displayed a similar pattern to R cells, with decreased ES and A5 usage and increased ATTS compared with N. No significant differences were detected between R and Het cells (**Fig 3B, S4C**).

We next evaluated the subcellular localization of proteins encoded by these differentially used transcripts. In the N vs R comparison, 44.1% of the proteins localized to the cytoplasm, lysosome, endoplasmic

reticulum, or Golgi apparatus; 29.6% nuclear; 8.1% were associated with the cell membrane; 7% were extracellular; and 4.3% mitochondrial (**Fig 3C**). Similarly, in N vs Het, 45.1% of proteins localized to the cytoplasm and cytoplasmic organelles; 29.7% nuclear; 11% associated with the cell membrane; 8.8% extracellular and 1.1% mitochondrial (**Fig S4D**). Because many cytoplasmic and membrane-localized proteins are involved in cell morphology and ECM production, we reasoned that these may reflect downstream phenotypic changes in R VSMCs rather than direct upstream regulators. To identify potential transcriptional regulators influenced by differential isoform usage, we therefore focused on transcripts encoding nuclear-localized proteins in the N vs R and N vs Het comparisons. In N vs. R, we identified altered isoform usage in several transcription factors and cofactors (DDX5, TAF2, PPRC1, MTA3, HOXA10, ZEB2, BTAF1, GPBP1), RNA metabolism proteins and splicing factors (HEATR1, PUM2, DDX5, ZC3H11A, PUF60, SRSF1, IMP4), RNA binding proteins (LUC7L2, WDR43, WR3) and chromatin associated/modifying enzymes (DNMT3B, SET, KDM4A, LMNA) (**Fig 3C**). These findings suggest that haplotype-specific isoform regulation at 9p21.3 may exert broad effects on transcriptional programs and gene regulatory networks. Chromosome 9–specific DTU analysis identified IL11RA, SET, UNC13B, and SLC25A25 as significantly altered at the isoform level in N vs. R, while only NCBP1 and MED22 exhibited significant isoform changes in N vs. Het (**Fig. S3B–D**). No significant changes were observed in the R vs. Het comparison (**Fig S3B**).

DTU analysis of CAD-GWAS genes highlighted several notable candidates, including DDX5, LDLR, LOX, and FN1, suggesting isoform-level regulatory effects linked to the 9p21.3 haplotype (**Fig 3D, FigS4E-H**). Interestingly, we detected four distinct coding isoforms of the LDLR, with imbalanced usage across N and R or Het VSMCs (**Fig 3E**). Isoform LDLR-208 (ENST00000558518.6) was significantly more abundant in Het VSMCs compared to N, with a similar trend in R VSMCs. Conversely, a novel isoform identified in our dataset (NT59183559) was markedly depleted in R and Het cells compared to N VSMCs (**Fig 3F**). The remaining two isoforms (LDLR-207 and NT199034250) were equally expressed across the genotypes (**Fig 3E-F**). Collectively, these findings demonstrate that the 9p21.3 locus influences both transcription and splicing of numerous CAD-associated genes and transcriptional regulators, suggesting the presence of a coordinated regulatory network that may contribute to susceptibility to plaque formation and progression. Importantly, because these changes occur without corresponding shifts in total gene expression, our work reveals a previously unrecognized signature of 9p21.3-driven CAD-associated transcript alterations not captured in earlier studies of the 9p21.3 locus.

The helicase DDX5 is a novel downstream effector of the 9p21.3 risk locus

Two independent analyses—DTU profiling and CAD-related transcript expression/usage—identified DEAD-box helicase 5 (DDX5) as a leading candidate affected by 9p21.3 haplotype–specific regulation. DDX5 has previously been implicated in cardiac function and heart failure[36]. We therefore sought to investigate its role in the 9p21.3-dependent VSMC phenotype and to interrogate DDX5 as a potential

downstream effector of this locus. Although overall DDX5 gene expression did not differ significantly between N and R or Het VSMCs, analysis of isoform proportion across the three major isoforms — two coding (DDX5-201/ENST00000225792.10, DDX5-201-0/ENST00000225792.10-0) and one nonsense-mediated decay (NMD)-sensitive isoform (DDX5-215/ENST00000581230.5) — revealed clear genotype-specific differences (**Fig 4A-B**). Both R and Het cells preferentially expressed the coding isoform DDX5-201 and showed significant downregulation of the NMD-sensitive isoform DDX5-215. Consistently, isoform-usage analysis demonstrated preferential usage of DDX5-215 in N VSMCs and of DDX5-201 in R and Het VSMCs (**Fig 4B**). To validate these findings, we performed additional iPSC-to-VSMC differentiation experiments and isoform-specific qPCR targeting DDX5-201. This analysis confirmed significant upregulation of DDX5-201 in R and Het VSMCs compared with N (**Fig 4C**).

To test whether DDX5 isoform modulation causally contributes to the R VSMCs phenotype, we combined our iPSC-derived VSMC model with CRISPR interference (CRISPRi). We assayed established signature genes of the aberrant R phenotype, including ANRIL short isoforms and the osteochondrogenic markers SOX9 and CYTL1[19] . R VSMCs were transduced with a dual-vector system expressing dCas9-KRAB and a DDX5-targeting guide RNA with parallel TdTomato expression for live-cell assessment (**Fig. 4D-E, S5A**). Following effective DDX5 knockdown, compared to cells not transduced (NT) or transduced with dCas9-KRAB only (dCas9) (**Fig. 4E, S5A**), we examined GATA6[32] , a known downstream target (**Fig. 4E**), and observed significant downregulation. Remarkably, suppression of DDX5 resulted in a substantial reduction in short ANRIL isoforms, while long ANRIL isoforms remained unchanged (**Fig. 4F**). We next assessed whether DDX5 knockdown was sufficient to attenuate expression of osteochondrogenic markers. Remarkably, both SOX9 and CYTL1 showed significant downregulation (**Fig. 4G**). We also examined the expression of splicing factors identified in our discovery analysis (NOVA1 and PTBP2) and found that both were downregulated upon DDX5 knockdown, suggesting that DDX5 isoform composition functions upstream of broader splicing alterations (**Fig. 4H**). Consistent with this model, overexpression of NOVA1 or PTBP2 in N VSMCs did not affect DDX5 expression (**Fig. S5B–C**), confirming that DDX5 acts upstream of these splicing regulators. Collectively, these results demonstrate that modulation of DDX5 is sufficient to influence the 9p21.3 risk-haplotype–specific VSMC phenotype and identify DDX5 as a key regulator of osteochondrogenic phenotypic modulation associated with this locus. To enhance the translational relevance of our findings, we queried a single-cell atlas of splicing isoforms from healthy human hearts[37] to assess DDX5 isoform expression in smooth muscle cells. Notably, DDX5-215, the non-coding, NMD-sensitive isoform detected in our Isoseq dataset, was the most abundant DDX5 transcript in healthy heart VSMCs. In our system, DDX5-215 is the most abundant isoform in N VSMCs, similarly to healthy heart SMCs (**Fig. 4I**). In contrast, R VSMCs show a significant reduction of the healthy DDX5-215 isoform, with parallel increase of DDX5-201, low abundant in healthy human hearts, suggesting an aberrant novel CAD-associated signature.

Discussion

The 9p21.3 coronary artery disease (CAD) risk locus has been extensively replicated across multiple GWAS as a major genomic region associated with increased CAD risk in diverse human populations[9–12,38,39]. Although identified nearly two decades ago, the functional mechanisms of this locus remain challenging to decipher. Over the past decade, our group and others have sought to unravel this genomic enigma using various approaches. Most studies have focused on establishing associations between 9p21.3 genotypes and cellular phenotypes, employing both vascular and non-vascular cell types as well as human tissues[40–46]. Modeling this locus in mice has proven difficult, as the syntenic region in mice lack the typical human haploblock of SNPs and an accurately annotated homolog of ANRIL, the lncRNA encoded within the human locus[40,47].

Our group was the first to generate a human-specific knockout model of the 9p21.3 locus and thereby demonstrated a clear genotype-to-phenotype causal effect of the 9p21.3 CAD risk locus in vascular smooth muscle cells (VSMCs), leveraging induced pluripotent stem cells (iPSCs), haplotype editing, and the generation of an isogenic iPSC collection. In our previous studies we demonstrated that the 9p21.3 risk haplotype impacts VSMC plasticity, and drives VSMCs to acquire an osteochondrogenic gene signature, along with increased calcification propensity and reduced migratory capacity[19] . Complete knockout of both copies of the risk haplotype restores the non-risk phenotype in iPSC-VSMCs. Notably, previous studies have linked the 9p21.3 CAD risk locus to a greater extent of calcification in atherosclerotic plaques from homozygous risk individuals compared with homozygous non-risk donors[48] . These findings suggest that our molecular and cellular readouts may explain tissue-level phenotypes observed in CAD patients.

While this system enabled us to establish the causal role of 9p21.3 in promoting vascular calcification—a hallmark of atherosclerotic plaques—the precise role of the risk versus non-risk haplotypes within an identical genetic background remains essential to define. Understanding both loss- and gain-of-function effects, as well as dominant and recessive haplotype interactions, is critical for elucidating disease mechanisms in relevant cell types.

To address this gap, we developed a powerful platform combining haplotype-biased editing, VSMC differentiation and long-read RNA sequencing. Our study provides new insights on how the 9p21.3 CAD locus shapes VSMC phenotypic shift through massive reprogramming of splicing events in the entire transcriptome leading to a disease-prone VSMC state.

Using this platform, we demonstrated that the risk haplotype at 9p21.3 exerts a dominant effect on VSMC phenotypes over the non-risk allele, concordant with the increased risk of disease in heterozygous individuals[9–11] . The gain-of-function phenotype driven by the risk haplotype persists even in heterozygous settings. This is the first isogenic system capable of showing how the two distinct 9p21.3 haplotypes determine different cell state programs. Although minimal, we also found a different transcriptional signature of VSMCs carrying only the R allele versus VSMCs carrying both R and N alleles (Het).

Building on our previous work, we now reveal a transcriptional landscape at isoform-level resolution, presenting the first long-read sequencing dataset of VSMCs carrying distinct 9p21.3 haplotypes. We identified thousands of differentially expressed transcripts—far beyond those reported previously—providing an unprecedented molecular signature of this locus.

Among other genes, our analyses revealed that the two 9p21.3 haplotypes exert a divergent regulatory effect on the expression of APELA (ELA/ELABELA) in VSMCs. APELA, a recently identified endogenous ligand of the Apelin receptor (APLNR), is essential for coronary artery morphogenesis, vascular branching, and post-injury angiogenic remodeling. The allele-specific modulation of APELA by the 9p21.3 haplotype suggests a mechanistic link between this CAD risk locus and coronary artery remodeling capacity, potentially influencing the ability of vessels to recover and reorganize following injury or stress.

Through long-read sequencing, we discovered hundreds of novel transcripts, classified as NIC (Novel In Catalog) or NNIC (Novel Not in Catalog), involved in allele-specific gene expression. These novel isoforms offer exciting opportunities for functional studies on VSMC phenotypic modulation and may represent new molecular targets for vascular disease.

Importantly, our controlled isogenic system enabled accurate identification of numerous genes that maintain steady expression across haplotypes but exhibit profound isoform switching. This reveals complex regulation of transcript usage and alternative splicing driven by the 9p21.3 locus. Our data highlight the fine tuning of CAD risk loci beyond simple gene expression and open avenues to explore novel druggable targets to potentially regulate VSMC phenotypic changes in vascular disease by modulating specific isoform transcripts.

Our comparative analyses, using the most recent survey of CAD risk loci and putative causal genes, linked 9p21.3 risk-driven transcriptional changes to GWAS-identified CAD genes, unveiling a molecular network that connects the 9p21.3 locus to isoform-level regulation across CAD-associated genes, including LDLR, ANGPTL4, and PCSK9. These associations, undescribed thus far, hint at the 9p21.3 and other major genetic risk factors for CAD involved under the same gene program, potentially explaining the high impact of this locus in conferring disease risk.

We identified DEAD-box helicase 5 (DDX5) as a top candidate gene influenced by 9p21.3 allele-specific effects. Using CRISPRi, we validated DDX5 as a novel molecular marker of CAD predisposition. Although previously implicated in heart failure and cardiomyocyte physiology, the role of DDX5 in atherosclerosis predisposition has not been fully explored. We show that DDX5 exhibits 9p21.3 haplotype-specific isoform usage, and its downregulation in VSMCs alters ANRIL short isoform expression and reduces the osteochondrogenic transcriptional signature. This provides the first causal link between 9p21.3 and DDX5, implicating this RNA helicase and splicing factor as a key mediator of splicing alterations in VSMCs. Interestingly, DDX5 has been recently linked to osteoarthritis, where its downregulation elicits expression of mesenchymal genes in chondrocytes[49] . Our study shows the reverse effect, where increased expression of DDX5 in mesenchymal cells (VSMCs) elicits an increased expression of osteochondrogenic

genes, suggesting a role for DDX5 as a keeper of VSMC-osteochondrogenic-like cells fate and suggest this RNA helicase as potential cell fate driver of VSMCs phenotypic modulation. Hence, targeting of DDX5 could be adopted to tackle arterial calcification. Importantly, our data reveal that N iPSC-VSMCs exhibit a transcriptomic signature consistent with healthy human heart SMCs, in agreement with the latest atlas of human heart isoform composition[37] . In contrast, depletion of the healthy DDX5-215 isoform, accompanied by increased proportion of the DDX5-201 isoform in our R VSMCs—which is minimally detected in healthy human hearts—suggests a potential CAD-associated signature driven by the 9p21.3 risk haplotype. Although we validated DDX5 as a new 9p21.3 partner, additional studies are needed to explore other splicing factors — potentially including other DDX family proteins — that may interact with ANRIL to coordinate VSMC transcriptomic regulation. We speculate that the 9p21.3 haplotypes influence DDX5 splicing and expression through long-range chromatin interactions. Our analyses revealed an enrichment of differential transcript expression on chromosomes 17 (where DDX5 is located), suggesting that the risk haplotype at 9p21.3 may engage in alternative chromatin contacts at specific hotspots in the genome.
Lastly, our study provides a valuable resource for the community to pursue follow-up investigations focused on 9p21.3-caused allelic imbalance of hundreds of transcripts across the genome.
In summary, we present a study with a novel, high-resolution dissection of the transcriptional complexity guided by the 9p21.3 CAD locus in VSMCs. This system reveals a new transcriptional signature underlying the osteochondrogenic switch of VSMCs and identifies DDX5 as a previously unrecognized partner of the 9p21.3 locus mediating these effects.

Materials & Methods

Data availability

Long-read bulk RNA sequencing datasets are deposited in GEO (GSE312611) and will be publicly available as of the date of the publication. All other data supporting the findings in this study are included in the main article and associated Supplementary materials. Unedited iPSC lines SCRP2411i (Cell Line Alias: KBET2411i) (RRID: CVCL_JV64) are available at WiCell in the NHLBI Next Gen - coronary artery disease and myocardial infarction (Dr. Eric Topol, Scripps Research Institute) collection.

Ethical compliance and cell lines

The authors have complied with all ethical regulations. All iPSC lines used in this study were previously derived and characterized under a study approved by the Scripps Research Institute IRB (IRB#115676, IRB#07-4714)[50]. The cells were transferred and maintained under a study approved by the University of Wisconsin-Madison through a Material Transfer Agreement (MSN246500). The iPSC lines included in this study were generated from Peripheral Blood Mononuclear cells (PBMCs) from blood donors consented under the IRB#115676, IRB#07-4714. All iPSC lines used derive from male donors: HE554 (SCRP2411i; Cell Line Alias: KBET2411i) (RRID: CVCL_JV64); C512 (SCRP0517i; Cell Line Alias: KBET0517i) (RRID:

CVCL_JV34); and HE463 (SCRP2307i; Cell Line Alias: KBET2307i) (RRID: CVCL_JV60). The choice to restrict this study to male donors was made to ensure line stability in relation to X inactivation, which can spontaneously change in female iPSC lines. Our study was not designed to detect sex-based phenotypes, and sex was not a determinant in our experiments. We have based our decision to exclude sex from consideration on the CAD GWAS data available thus far, which shows no compelling evidence of sex differences in 9p21.3-based risk of CAD.

Published dataset analysis

The dataset from Lo Sardo et al. is available GEO: GSE120099

Heatmaps: Heatmaps of published data were generated using the heatmap.2 command from the ggplot2 package (v3.5.1).
Volcano plots: Volcano plots of published data were generated using the ggplot command, also from the ggplot2 package.
Gene Ontology (GO) Enrichment Analysis: GO analysis was conducted using the clusterProfiler package (v3.0.4, RRID:SCR_016884).

iPSC derivation, differentiation and maintenance

iPSCs were cultured on Matrigel-coated (Corning 354277) cell culture plates and mTeSR (Stem Cell Technologies cat. 85850), cultured at 37°C under normoxic conditions (20% O_2) with 5% CO_2. iPSCs were differentiated into VSMCs as previously described (Sardo et al. 2018; Cheung et al. 2014) . VSMCs were maintained on VSMC media (DMEM, Gibco 11965092; 10% BenchMark™ Fetal Bovine Serum, Gemini; Glutamax, Gibco 35050061; Penicillin/Streptomycin, Gibco 15140122; MEM Non-Essential Amino Acids, Gibco 11140050).

Generation of hemizygous iPSC

Isogenic hemizygous lines were generated from a male heterozygous donor at the 9p21.3 locus (carrying one risk and one non-risk allele) by TALEN-mediated haplotype editing as we previously described and validated. After single cell subcloning and iPSC clone expansion, genotyping was performed by primer sequences including: GJC 344F (5′ CATACAGGTCCCTGGCACTAA 3′), GJC 346F (5′ CGAAGGGCTTCCCTGTCTA 3′), and 347R (5′ GACTTTCCCCCA CAATGAAA 3′). Genotyping PCR was performed using Q5 Hot Start DNA polymerase (NEB M0493S) in 25uL reactions. Reaction parameters include: 30 cycles, 58 °C annealing, 30sec extension, 200ng genomic DNA template per reaction, and primer concentration of 200nM each. Based on genotyping, we selected iPSC clones with deletion of either the risk or non-risk 9p21.3 locus, confirmed by Sanger sequencing for SNPs rs1333049 and rs10757278.

Long-read bulk RNA sequencing

Total RNA samples submitted to the University of Wisconsin-Madison Biotechnology Center Gene Expression Center (*RRID:SCR_017757)* were assayed on NanoDropOne Spectrophotometer and Agilent 4200Tapestation to assess purity and integrity. RNA concentrations were accurately quantified by Qubit 4.0. RNA samples with RIN > 9 were selected for library construction. 300ng total RNA was converted to single-stranded cDNA and amplified using the Iso-Seq Express 2.0 Kit (Pacific Biosciences). Iso-Seq libraries were constructed with the SMRTbell Template Prep Kit 3.0 (Pacific Biosciences). Library quantity and quality were assessed by Qubit 4.0 and Agilent 4200Tapestation, respectively. Libraries were sequenced on one PacBio Revio SMRT cell. Revio polymerase kit v1.0 and Revio SMRT cell v1.0 used (Pacific Biosciences). Library prep and sequencing were conducted at the Gene Expression Core of the Biotechnology Center at UW-Madison.

Bioinformatic analysis of long-read bulk RNA sequencing

All codes and scripts used in this study are available at https://github.com/LoSardo-Lab.

Isoform Discovery and Alignment

We identified and characterized gene isoforms from PacBio HiFi reads using the IsoSeq v4.3 pipeline. First, the initial processing of the raw BAM files began with the *lima* tool to identify and trim the 5' and 3' cDNA primers. This step also used the embedded barcode sequences to demultiplex the pooled sequencing data into sample-specific files. These full-length reads then underwent further cleaning with *isoseq refine*. This step identifies and trims the 3' poly(A) tail and detects and splits artificial concatemers—ligation artifacts where multiple distinct cDNA molecules are sequenced as a single long read. The resulting full-length, non-concatemer (FLNC) reads were then subjected to de novo clustering with *isoseq cluster2*. This reference-free step groups reads originating from the same isoform to generate a highly accurate polished consensus sequence. These polished isoforms were subsequently aligned to the hg38 human reference genome (GENCODE v39) using *isoseq pbmm2*, an aligner optimized for long-read data. Finally, to create a non-redundant transcript set, *isoseq collapse* was used to merge isoforms that were splice-compatible, meaning they shared identical splice junctions but differed only in their 5' or 3' ends, which often reflects natural transcriptional start site variability.

Classification and Filtering

With a set of unique isoforms defined, we performed structural annotation and rigorous quality control using the *isoseq pigeon* toolkit. The *pigeon classify* command categorized each isoform by comparing its splice junctions against the reference annotation, using the established SQANTI classification system (Pardo-Palacios et al. 2024). This process assigned labels such as Full Splice Match (FSM) for isoforms identical to known transcripts, Incomplete Splice Match (ISM) for partial matches, Novel in Catalog (NIC) for new combinations of known splice sites, and Novel Not in Catalog (NNC) for isoforms containing at

least one previously unannotated splice site. To ensure the final dataset's integrity, pigeon filter was applied to remove common long-read sequencing artifacts. This filtering specifically targeted isoforms resulting from intra-priming, where the oligo(dT) primer mistakenly anneals to an internal A-rich sequence instead of the true poly(A) tail, and reverse transcriptase (RT) template switching, which creates chimeric cDNAs. The process also removed isoforms with poor read support for non-canonical splice junctions, yielding a final, high-confidence catalog of transcripts.

Differential Expression and Functional Analysis

We performed differential expression analysis at both the gene and transcript levels using the edgeR v4.6 package in R (Chen et al. 2025). The analysis began with a read count matrix generated by the FLAIR v2.2 pipeline (Tang et al. 2020), which quantifies isoform expression from full-length transcript sequencing data. We derived gene-level counts by aggregating the counts of all constituent isoforms for each gene. To enhance statistical power and remove noise from lowly expressed features, we first filtered the data, retaining only those genes and transcripts that had at least two counts in a minimum of two samples. The core differential analysis was then conducted within the edgeR framework, which models the count data using a negative binomial distribution to appropriately account for the overdispersion typically seen in sequencing data. After normalizing for library size and composition using the Trimmed Mean of M-values (TMM) method, we fit a generalized linear model (GLM) to identify significant expression changes. Significance was determined based on a False Discovery Rate (FDR) cutoff of 0.05, which corrects for multiple hypothesis testing. To summarize the overall expression, change at the gene level while considering the contributions of different isoforms, we calculated a weighted mean $\log_2$ fold change (LFC) for each gene. This was done by weighting the LFC of each individual isoform by its average normalized expression (baseMean), giving more influence on the more abundant isoforms. Finally, to understand the biological implications of these expression changes, we performed a functional enrichment analysis on the list of significant genes using the clusterProfiler package v4.0 (Wu et al. 2021).

Differential Transcript Usage and Functional Consequence Analysis

This analysis was conducted using the IsoformSwitchAnalyzeR v2 R package(Vitting-Seerup and Sandelin 2019), a comprehensive toolkit for identifying and characterizing isoform switching events. We began by importing the isoform-level read counts, a GTF file defining transcript structures, and isoform nucleotide sequences generated by the FLAIR pipeline. These data sources were integrated into a switchAnalyzeRlist object, the central data structure for the analysis. A pre-filtering step was applied to remove genes with low expression, thereby increasing the statistical power to detect genuine switching events. The core statistical test for DTU was performed by leveraging the power of the DEXSeq package, which is designed to detect changes in feature usage relative to the parent gene's total expression. This method, combined with

limma's empirical Bayes approach for variance moderation (Ritchie et al. 2015), with significance defined by FDR < 0.05.

Beyond statistical significance, we aimed to understand the functional consequences of these isoform switches. First, we predicted the Open Reading Frames (ORFs) for all isoforms to determine their protein-coding sequences. We then used a suite of specialized tools to predict functional attributes of the resulting proteins. This included assessing the coding potential of each transcript with CPAT v3.0.5(Wang et al. 2013), identifying conserved functional protein domains with Pfam v37.2 (Punta et al. 2012), and predicting signal peptides for secretion using SignalP v6.0(Della Marina et al. 2024). We also analyzed protein topology by predicting transmembrane helices with DeepTMHMM v1.0.24("DeepTMHMM Predicts Alpha and Beta Transmembrane Proteins Using Deep Neural Networks - Abstract - Europe PMC," n.d.), identified intrinsically disordered regions with IUPred2A (Mészáros et al. 2018), and predicted the final sub-cellular localization of the proteins with DeepLoc2 v2.1 (Thumuluri et al. 2022). Finally, we used the extractTopSwitches function to extract the most biologically relevant events. This function filters for switches that were not only statistically significant (FDR < 0.05) but also showed a substantial change in proportional expression (an isoform fraction difference > 0.1) and resulted in a predicted functional change.

DDX5 Perturbation

gRNA design and cloning for DDX5: A plasmid containing the KRAB domain fused to dCas9 and the vector to clone sgRNA were obtained from Addgene (RRID: Addgene_99372 and Addgene_99376) (PMID:28757163). The plasmid #99376 contains a dTomato fluorescent protein. DDX5 sgRNA was custom designed by using the CHOPCHOP algorithm design tool. Forward and reverse guides of each target were used to generate duplexes and ligated into the *BsmBI* vector (Xing et al., 2014). The sgRNA cloned in the vector #99376 was confirmed by Sanger sequencing.

*lenti-EF1a-dCas9-KRAB-Puro was a gift from Kristen Brennand (Addgene plasmid #99372; http://n2t.net/addgene:99372; RRID: Addgene_99372)

*lentiGuide-Hygro-dTomato was a gift from Kristen Brennand (Addgene plasmid #99376: http://n2t.net/addgene:99376; RRID: Addgene _99376)

Overexpression of splicing genes

Cloning of NOVA1 and PTBP2 gene into TetO MCS: cDNA using SuperScript IV First Strand Synthesis System (Cat # 18091050) was synthesized using 1ug of total RNA. 100ng of the synthesized cDNA was used to set up a PCR using primer sequences that include:

For NOVA1 gene: NOVA1_XbaI_Kozak_Fw (5' GAATCTAGAGCCACCATGATGGCGGCAGCTCCCAT 3'), NOVA1_NheI_Rv (5' AGAGCTAGCTCAACCCACTTTCTGAGGAT 3'). PCR was performed using Q5 Hot Start DNA polymerase (NEB M0493S) in 50uL reaction. Reaction parameters include: 10 cycles 64°C

annealing, 60sec extension, 25 cycles 72°C annealing, 60sec extension, and primer concentration of 500nM each.

For PTBP2 gene: PTBP2_XbaI_Kozak_Fw (5' GAATCTAGAGCCACCATGGACGGAATCGTCACTGA 3'), PTBP2_NheI_Rv (5' AGAGCTAGCTTAAATTGTTGACTTGGAGA 3'). PCR was performed using Q5 Hot Start DNA polymerase (NEB M0493S) in 50uL reaction. Reaction parameters include: 10 cycles 57°C annealing, 60sec extension, 25 cycles 68°C annealing, 60sec extension, and primer concentration of 500nM each.

PCR amplicons were excised from agarose gels and purified using the QIAquick Gel Extraction Kit (Cat. #28704). The purified products were cloned into the Zero Blunt TOPO PCR Cloning vector (Cat. #450245) according to the manufacturer's protocol. Plasmids were isolated from selected TOPO clones by miniprep to obtain inserts for subsequent subcloning.

For restriction-based cloning, 2 µg of the TOPO plasmid containing the target gene and 1 µg of the FUW-tetO-MCS backbone (RRID: Addgene_84008; PMID: 27641305) were digested with XbaI and NheI. Digested products were purified and ligated at a 1:3 (vector: insert) molar ratio using T4 DNA ligase (NEB M0202S). Positive clones were screened by diagnostic restriction digestion, and insert identity was verified by plasmid sequencing (Plasmidsaurus).

Lentiviral preparation and infection: To prepare lentivirus, HEK293T cells (ATCC, cat #: CRL-11268) (RRID: CVCL_1926) at 60% confluency were transfected with 3rd generation packaging vectors (REV, RRE, and pMD 2.G) (RRID: Addgene_12253, Addgene_12251 and Addgene_12259), dCas9-KRAB and DDX5 gRNAs plasmids using the calcium phosphate method. 24 hours after transfection, the media was replaced. Virus was harvested 24 hrs after the media change (48 hrs after transfection). After filtering through 0.45µm low protein-binding syringe filters (SLHVM33RS Millipore), supernatant containing the viral particles was stored at -80℃. Cells were infected and treated with Puromycin 1µg/mL and Hygromycin 200 µg /mL concentration for 48 hrs. The antibiotics were added 48 hours after infection.

Immunocytochemistry

Cells were first fixed using 4% paraformaldehyde (15710 Electron Microscopy Science) in PBS. The fixed samples were incubated with 0.5% Triton X-100 (T8787 Sigma-Aldrich) in PBS for 10 minutes. 5% FBS (100-106 Gemini Bio) in PBS was used for blocking for 1 hour at RT. Primary antibodies against Nanog (Abcam Cat# ab21624, RRID: AB_446437) for iPSCs marker and CNN (Sigma-Aldrich Cat# C2687, RRID: AB_476840) and TAGLN (Abcam Cat# ab14106, RRID: AB_443021) for VSMCs marker diluted in blocking buffer were incubated for approximately 2 hours at room temperature or overnight at 4°C. After three PBS washes, the secondary antibodies Donkey anti-mouse 488 (Alexa-fluor A32766 Invitrogen, RRID: AB_2762823), Donkey anti-rabbit 555 (Alexa-fluor A32794 Invitrogen, RRID: AB2762834), and DAPI

(MBD0015 Sigma–Aldrich) in blocking buffer were added for 1 hour at RT. Three additional PBS washes were performed, and the cells were imaged.

RNA extraction, cDNA synthesis, and qPCR

The cell pellets were dissociated using TRIzol (15596018 Invitrogen). RNA was then extracted using a Zymo Direct-zol RNA Miniprep kit (R2052) according to the manufacturer's protocol. iScript Reverse Transcription Reaction Mix (1708891, Bio-Rad) was used for cDNA synthesis. For qPCR, iTaq Universal SYBR Green Supermix (1725121 Bio-Rad) and SsoAdvanced Universal SYBR Green Supermix (17252721 Bio-Rad) was used on a Bio-Rad CFX OPUS 384 Touch Real-Time PCR machine. GraphPad Prism (RRID: SCR_002798) was used to perform statistical analysis using unpaired t-tests or 1-way ANOVA with Bonferroni correction. A complete list of primers used for qPCR is provided below.

Statistical analysis

Details of statistical analyses are given in the Figure Legends. These include the number of samples and the number of independent experiments. Data were analyzed using unpaired t-test or one-way ANOVA with Bonferroni multiple comparison post hoc test as specified in the corresponding figure legends.

Primer Table

Target	Primer	Sequence
PPIA	hPPIA Fwd	5'- CCGAGGAAAACCGTGTACTATTAG -3'
	hPPIA Rev	5'- TGCTGTCTTTGGGACCTTG -3'
ANRIL Short	ANRIL Short Fwd	5'- ACACATCAAAGGAGAATTTTCTTGG -3'
	ANRIL Short Rev	5'- GTACTGACTCGGGAAAGGATTC -3'
ANRIL Long	ANRIL Long Fwd	5'- GCACACTGGTCAGCTGTTTT -3'
	ANRIL Long Rev	5'- ACTTTTCATCTTTCTGTATTTCAA -3'
DDX5 Guide CRISPRi	Oligo Fw	5'-caccgGTCACTCGAATAACCCGACATGG-3'
	Oligo Rv	5'-aaacCCATGTCGGGTTATTCGAGTGACc-3'
GJC 344	GJC 344 Fw	5'-CATACAGGTCCCTGGCACTAA-3′
GJC 346	GJC 346 Fw	5′ -CGAAGGGCTTCCCTGTCTA -3′
GJC 347	GJC 347 Rv	5′ -GACTTTCCCCCA CAATGAAA-3'
SOX9	hSOX9 Fw	5'-ACTTGCACAACGCCGAG-3'
	hSOX9 Rv	5'-CTGGTACTTGTAATCCGGGTG-3'
COL2A1	COL2A1 Fw	5'-AAGACGTGAAAGACTGCCTC-3'
	COL2A1 Rv	5'-TTCTCCTTTCTGTCCCTTTGG-3'
NOVA1	NOVA1 Fw	5'-TTGCCATCTTCCCCAACTAC-3'

	NOVA1 Rv	5'-TTACAGCCTTCACAGTAGCAC-3'
KHDRBS2	KHDRBS2 Fw	5'-CCAACAGTGCCAGGATACAG-3'
	KHDRBS2 Rv	5'-CTTTGTGTTTGGGTCGCATAG-3'
PTBP2	PTBP2 Fw	5'-AATGAAGAGATGGTTACGCCC-3'
	PTBP2 Rv	5'-GGCAAGTTGTGATTGGTTTCC-3'
RBM20	RBM20 Fw	5'-ATCATACGTGCCCATTCCAG-3'
	RBM20 Rv	5'-TCATTCTCAGTGCAGCTTCC-3'
DDX5	DDX5 Fw	5'-AGCGTGACTGGGTTCTAAATG-3'
	DDX5 Rv	5'-AGGAGTTAGGGTAGTCATAATTGATG-3'
GATA6	GATA6 Fw	5'-AACACAACCTACAGCCTCAG-3'
	GATA6 Rv	5'-TCTTGACCCGAATACTTGAGC-3'
CYTL1	CYTL1 Fw	5'-TGAAGGACAAAGCACGGAAG-3'
	CYTL1 Rv	5'-GTAGTCACTGGGATTGGGTATTC-3'
NOVA1 OE	NOVA1-XbaI FW	5'- GAATCTAGAGCCACCATGATGGCGGCAGCTCCCAT -3'
	NOVA1-NheI Rv	5'- AGAGCTAGCTCAACCCACTTTCTGAGGAT -3'
PTBP2 OE	PTBP2-XbaI Fw	5'- GAATCTAGAGCCACCATGGACGGAATCGTCACTGA -3'
	PTBP-NheI Rv	5'- AGAGCTAGCTTAAATTGTTGACTTGGAGA -3'

Acknowledgments

The authors utilized the University of Wisconsin – Madison Biotechnology Center Gene Expression Center Core Facility (Research Resource Identifier – RRID:SCR_017757).

Author contribution

Conceptualization, S.S., H.Y. and V.L.S. Data curation, S.S. and H. Y. Formal analysis and Methodology, S.S., H.Y., E. S. and K.M. Manuscript writing and data visualization S.S, H.Y and V.L.S.

Source of funding

The authors acknowledge the following funding: S.S. was supported by the UW Stem Cell and Regenerative Medicine Center Graduate training award. E.S. was supported by the NIH T32 Genetics Training grant (T32GM007133) and Advanced Opportunity Fellowship through SciMed Graduate Research Scholars, and the CVRC T32 at the University of Wisconsin Madison. This work was supported by the National Institute of Health grants R35GM155127 (VLS) and the Wisconsin Partnership Program New Investigator Award (VLS). V.L.S. also received funding for this study from the University of Wisconsin Madison School of Medicine and Public Health.

Disclosure

Nothing to disclose.

REFERENCES

1. Martin SS, Aday AW, Almarzooq ZI, Anderson CAM, Arora P, Avery CL, Baker-Smith CM, Gibbs BB, Beaton AZ, Boehme AK, et al. 2024 Heart Disease and Stroke Statistics: A Report of US and Global Data From the American Heart Association. *Circulation*. 2024;149:e347–e913.

2. Myers RH, Kiely DK, Cupples LA, Kannel WB. Parental history is an independent risk factor for coronary artery disease: The Framingham Study. *Am Heart J*. 1990;120:963–969.

3. Marenberg ME, Risch N, Berkman LF, Floderus B, Faire U de. Genetic Susceptibility to Death from Coronary Heart Disease in a Study of Twins. *New Engl J Medicine*. 1994;330:1041–1046.

4. Lloyd-Jones DM, Nam B-H, D'Agostino SRB, Levy D, Murabito JM, Wang TJ, Wilson PWF, O'Donnell CJ. Parental Cardiovascular Disease as a Risk Factor for Cardiovascular Disease in Middle-aged Adults: A Prospective Study of Parents and Offspring. *Jama*. 2004;291:2204–2211.

5. Won H-H, Natarajan P, Dobbyn A, Jordan DM, Roussos P, Lage K, Raychaudhuri S, Stahl E, Do R. Disproportionate Contributions of Select Genomic Compartments and Cell Types to Genetic Risk for Coronary Artery Disease. *Plos Genet*. 2015;11:e1005622.

6. Münzel T, Hahad O, Sørensen M, Lelieveld J, Duerr GD, Nieuwenhuijsen M, Daiber A. Environmental risk factors and cardiovascular diseases: a comprehensive expert review. *Cardiovascular Research*. 2022;118:2880–2902.

7. Erdmann J, Kessler T, Venegas LM, Schunkert H. A decade of genome-wide association studies for coronary artery disease: the challenges ahead. *Cardiovasc Res*. 2018;114:1241–1257.

8. Kessler T, Schunkert H. Coronary Artery Disease Genetics Enlightened by Genome-Wide Association Studies. *Jacc Basic Transl Sci*. 2021;6:610–623.

9. Samani NJ, Erdmann J, Hall AS, Hengstenberg C, Mangino M, Mayer B. Genomewide Association Analysis of Coronary Artery Disease. *New England Journal of Medicine* [Internet]. 2007;1–11. Available from: http://www.nejm.org/doi/pdf/10.1056/NEJMoa072366

10. McPherson R, Pertsemlidis A, Kavaslar N, Stewart A, Roberts R, Cox DR, Hinds DA, Pennacchio LA, Tybjaerg-Hansen A, Folsom AR, et al. A common allele on chromosome 9 associated with coronary heart disease. *Science*. 2007;316:1488–1491.

11. Helgadottir A, Thorleifsson G, Manolescu A, Gretarsdottir S, Blondal T, Jonasdottir A, Jonasdottir A, Sigurdsson A, Baker A, Palsson A, et al. A common variant on chromosome 9p21 affects the risk of myocardial infarction. *Science*. 2007;316:1491–1493.

12. Tcheandjieu C, Zhu X, Hilliard AT, Clarke SL, Napolioni V, Ma S, Lee KM, Fang H, Chen F, Lu Y, et al. Large-scale genome-wide association study of coronary artery disease in genetically diverse populations. *Nat Med*. 2022;1–13.

13. Aragam KG, Jiang T, Goel A, Kanoni S, Wolford BN, Atri DS, Weeks EM, Wang M, Hindy G, Zhou W, et al. Discovery and systematic characterization of risk variants and genes for coronary artery disease in over a million participants. *Nat. Genet.* 2022;54:1803–1815.

14. Assimes TL, Knowles JW, Basu A, Iribarren C, Southwick A, Tang H, Absher D, Li J, Fair JM, Rubin GD, et al. Susceptibility locus for clinical and subclinical coronary artery disease at chromosome 9p21 in the multi-ethnic ADVANCE study. *Human Molecular Genetics*. 2008;17:2320–2328.

15. Gränsbo K, Almgren P, Sjögren M, Smith JG, Engström G, Hedblad B, Melander O. Chromosome 9p21 genetic variation explains 13% of cardiovascular disease incidence but does not improve risk prediction. *J Intern Med*. 2013;274:233–40.

16. Holdt LM, Teupser D. Long Noncoding RNA ANRIL: Lnc-ing Genetic Variation at the Chromosome 9p21 Locus to Molecular Mechanisms of Atherosclerosis. *Frontiers in Cardiovascular Medicine*. 2018;5:145.

17. Kong Y, Hsieh C-H, Alonso LC. ANRIL: A lncRNA at the CDKN2A/B Locus With Roles in Cancer and Metabolic Disease. *Frontiers in endocrinology*. 2018;9:405.

18. LoSardo V, Chubukov P, Ferguson W, Kumar A, Teng EL, Duran M, Zhang L, Cost G, Engler AJ, Urnov F, et al. Unveiling the Role of the Most Impactful Cardiovascular Risk Locus through Haplotype Editing. *Cell*. 2018;175:1796-1810.e20.

19. Salido E, Vieira C de M, Mosquera JV, Zade R, Parikh P, Suryavanshi S, Miller CL, Sardo VL. The 9p21.3 Coronary Artery Disease Risk Locus Drives Vascular Smooth Muscle Cells to an Osteochondrogenic State. *Arter., Thromb., Vasc. Biol.* 2025;45:702–721.

20. Gao C, Ren S, Lee J-H, Qiu J, Chapski DJ, Rau CD, Zhou Y, Abdellatif M, Nakano A, Vondriska TM, et al. RBFox1-mediated RNA splicing regulates cardiac hypertrophy and heart failure. *J. Clin. Investig.* 2016;126:195–206.

21. Guo W, Schafer S, Greaser ML, Radke MH, Liss M, Govindarajan T, Maatz H, Schulz H, Li S, Parrish AM, et al. RBM20, a gene for hereditary cardiomyopathy, regulates titin splicing. *Nature Medicine*. 2012;18:766–773.

22. Lundberg AK, Jonasson L, Hansson GK, Mailer RKW. Activation-induced FOXP3 isoform profile in peripheral CD4+ T cells is associated with coronary artery disease. *Atherosclerosis*. 2017;267:27–33.

23. Babaev VR, Porro F, Linton MF, Fazio S, Baralle FE, Muro AF. Absence of regulated splicing of fibronectin EDA exon reduces atherosclerosis in mice. *Atherosclerosis*. 2008;197:534–540.

24. Mango R, Biocca S, Vecchio F del, Clementi F, Sangiuolo F, Amati F, Filareto A, Grelli S, Spitalieri P, Filesi I, et al. In Vivo and In Vitro Studies Support That a New Splicing Isoform of OLR1 Gene Is Protective Against Acute Myocardial Infarction. *Circ. Res.* 2005;97:152–158.

25. Giampietro C, Deflorian G, Gallo S, Matteo AD, Pradella D, Bonomi S, Belloni E, Nyqvist D, Quaranta V, Confalonieri S, et al. The alternative splicing factor Nova2 regulates vascular development and lumen formation. *Nat. Commun.* 2015;6:8479.

26. Griffin C, Saint-Jeannet J-P. Spliceosomopathies: Diseases and mechanisms. *Developmental dynamics : an official publication of the American Association of Anatomists*. 2020;249:1038–1046.

27. Lesurf R, Breckpot J, Bouwmeester J, Hanafi N, Jain A, Liang Y, Papaz T, Lougheed J, Mondal T, Alsalehi M, et al. A validated heart-specific model for splice-disrupting variants in childhood heart disease. *Genome Medicine*. 2024;16:119.

28. Jang MY, Patel PN, Pereira AC, Willcox JAL, Haghighi A, Tai AC, Ito K, Morton SU, Gorham JM, McKean DM, et al. Contribution of Previously Unrecognized RNA Splice-Altering Variants to Congenital Heart Disease. *Circulation: Genomic and Precision Medicine*. 2023;16:224–231.

29. Ortiz-Śanchez P, Villalba-Orero M ia, neta MML opez-Olã, Larrasa-Alonso J, anchez-Cabo F atima S, omez CM i-G\', Camafeita E, omez-Salinero J us MG, andez LR-H, Nielsen PJ, et al. Loss of SRSF3 in Cardiomyocytes Leads to Decapping of Contraction-Related mRNAs and Severe Systolic Dysfunction. *Circulation Research*. 2019;125:170–183.

30. Chang K-T, Cheng C-F, King P-C, Liu S-Y, Wang G-S. CELF1 Mediates Connexin 43 mRNA Degradation in Dilated Cardiomyopathy. *Circulation Research*. 2017;121:1140–1152.

31. Howson JMM, Zhao W, Barnes DR, Ho W-K, Young R, Paul DS, Waite LL, Freitag DF, Fauman EB, Salfati EL, et al. Fifteen new risk loci for coronary artery disease highlight arterial-wall-specific mechanisms. *Nature Genetics*. 2017;49:1113–1119.

32. Fan Y, Chen Y, Zhang J, Yang F, Hu Y, Zhang L, Zeng C, Xu Q. Protective Role of RNA Helicase DEAD-Box Protein 5 in Smooth Muscle Cell Proliferation and Vascular Remodeling. *Circ. Res.* 2019;124:e84–e100.

33. Chng SC, Ho L, Tian J, Reversade B. ELABELA: A Hormone Essential for Heart Development Signals via the Apelin Receptor. *Dev. Cell*. 2013;27:672–680.

34. Liu Q, Hu T, He L, Huang X, Tian X, Zhang H, He L, Pu W, Zhang L, Sun H, et al. Genetic targeting of sprouting angiogenesis using Apln-CreER. *Nat. Commun.* 2015;6:6020.

35. Sharma B, Ho L, Ford GH, Chen HI, Goldstone AB, Woo YJ, Quertermous T, Reversade B, Red-Horse K. Alternative Progenitor Cells Compensate to Rebuild the Coronary Vasculature in Elabela- and Apj-Deficient Hearts. *Dev. Cell*. 2017;42:655-666.e3.

36. Jia K, Cheng H, Ma W, Zhuang L, Li H, Li Z, Wang Z, Sun H, Cui Y, Zhang H, et al. RNA Helicase DDX5 Maintains Cardiac Function by Regulating CamkIIδ Alternative Splicing. *Circulation*. 2024;150:1121–1139.

37. Pan T, Lu L, Youker K, Shiau C-K, Wang M, Lin H-Y, Nguyen A, He Y, Tong E, Zhu P, et al. Single-Cell Splicing Isoform Atlas of the Adult Human Heart and Heart Failure. *Circulation*. 2025;152:1501–1514.

38. Koyama S, Ito K, Terao C, Akiyama M, Horikoshi M, Momozawa Y, Matsunaga H, Ieki H, Ozaki K, Onouchi Y, et al. Population-specific and trans-ancestry genome-wide analyses identify distinct and shared genetic risk loci for coronary artery disease. *Nat Genet*. 2020;52:1169–1177.

39. Vries PS de, Conomos MP, Singh K, Nicholson CJ, Jain D, Hasbani NR, Jiang W, Lee S, Cardenas CLL, Lutz SM, et al. Whole-genome sequencing uncovers two loci for coronary artery calcification and identifies ARSE as a regulator of vascular calcification. *Nat. Cardiovasc. Res.* 2023;2:1159–1172.

40. Jarinova O, Stewart AFR, Roberts R, Wells G, Lau P, Naing T, Buerki C, McLean BW, Cook RC, Parker JS, et al. Functional Analysis of the Chromosome 9p21.3 Coronary Artery Disease Risk Locus. *Arteriosclerosis, Thrombosis, and Vascular Biology*. 2009;29:1671–1677.

41. Liu Y, Sanoff HK, Cho H, Burd CE, Torrice C, Mohlke KL, Ibrahim JG, Thomas NE, Sharpless NE. INK4/ARF transcript expression is associated with chromosome 9p21 variants linked to atherosclerosis. *PLoS ONE*. 2009;4:e5027.

42. Holdt LM, Beutner F, Scholz M, Gielen S, Gäbel G, Bergert H, Schuler G, Thiery J, Teupser D. ANRIL expression is associated with atherosclerosis risk at chromosome 9p21. *Arteriosclerosis, Thrombosis, and Vascular Biology*. 2010;30:620–627.

43. Holdt LM, Hoffmann S, Sass K, Langenberger D, Scholz M, Krohn K, Finstermeier K, Stahringer A, Wilfert W, Beutner F, et al. Alu Elements in ANRIL Non-Coding RNA at Chromosome 9p21 Modulate Atherogenic Cell Functions through Trans-Regulation of Gene Networks. *PLoS Genetics* [Internet]. 2013;9:e1003588-12. Available from: http://www.ncbi.nlm.nih.gov/pmc/articles/PMC3701717/pdf/pgen.1003588.pdf

44. Almontashiri NAM, Antoine D, Zhou X, Vilmundarson RO, Zhang SX, Hao KN, Chen H-H, Stewart AFR. 9p21.3 Coronary Artery Disease Risk Variants Disrupt TEAD Transcription Factor–Dependent Transforming Growth Factor &bgr; Regulation of p16 Expression in Human Aortic Smooth Muscle Cells. *Circulation*. 2015;132:1969–1978.

45. Holdt LM, Sass K, Gäbel G, Bergert H, Thiery J, Teupser D. Expression of Chr9p21 genes CDKN2B (p15INK4b), CDKN2A (p16INK4a, p14ARF) and MTAP in human atherosclerotic plaque. *Atherosclerosis*. 2011;214:264–270.

46. Motterle A, Pu X, Wood H, Xiao Q, Gor S, Ng FL, Chan K, Cross F, Shohreh B, Poston RN, et al. Functional analyses of coronary artery disease associated variation on chromosome 9p21 in vascular smooth muscle cells. *Human Molecular Genetics* [Internet]. 2012;21:4021–4029. Available from: http://www.ncbi.nlm.nih.gov/pmc/articles/PMC3428153/pdf/dds224.pdf

47. He S, Gu W, Li Y, Zhu H. ANRIL/CDKN2B-AS shows two-stage clade-specific evolution and becomes conserved after transposon insertions in simians. *BMC evolutionary biology*. 2013;13:247.

48. Kojima Y, Ye J, Nanda V, Wang Y, Flores AM, Jarr K-U, Tsantilas P, Guo L, Finn AV, Virmani R, et al. Knockout of the Murine Ortholog to the Human 9p21 Coronary Artery Disease Locus Leads to Smooth Muscle Cell Proliferation, Vascular Calcification, and Advanced Atherosclerosis. *Circulation*. 2020;141:1274–1276.

49. Liu Q, Han M, Wu Z, Fu W, Ji J, Liang Q, Tan M, Zhai L, Gao J, Shi D, et al. DDX5 inhibits hyaline cartilage fibrosis and degradation in osteoarthritis via alternative splicing and G-quadruplex unwinding. *Nat. Aging*. 2024;4:664–680.

50. LoSardo V, Ferguson W, Erikson GA, Topol EJ, Baldwin KK, Torkamani A. Influence of donor age on induced pluripotent stem cells. *Nature Biotechnology*. 2016;35:69–74.

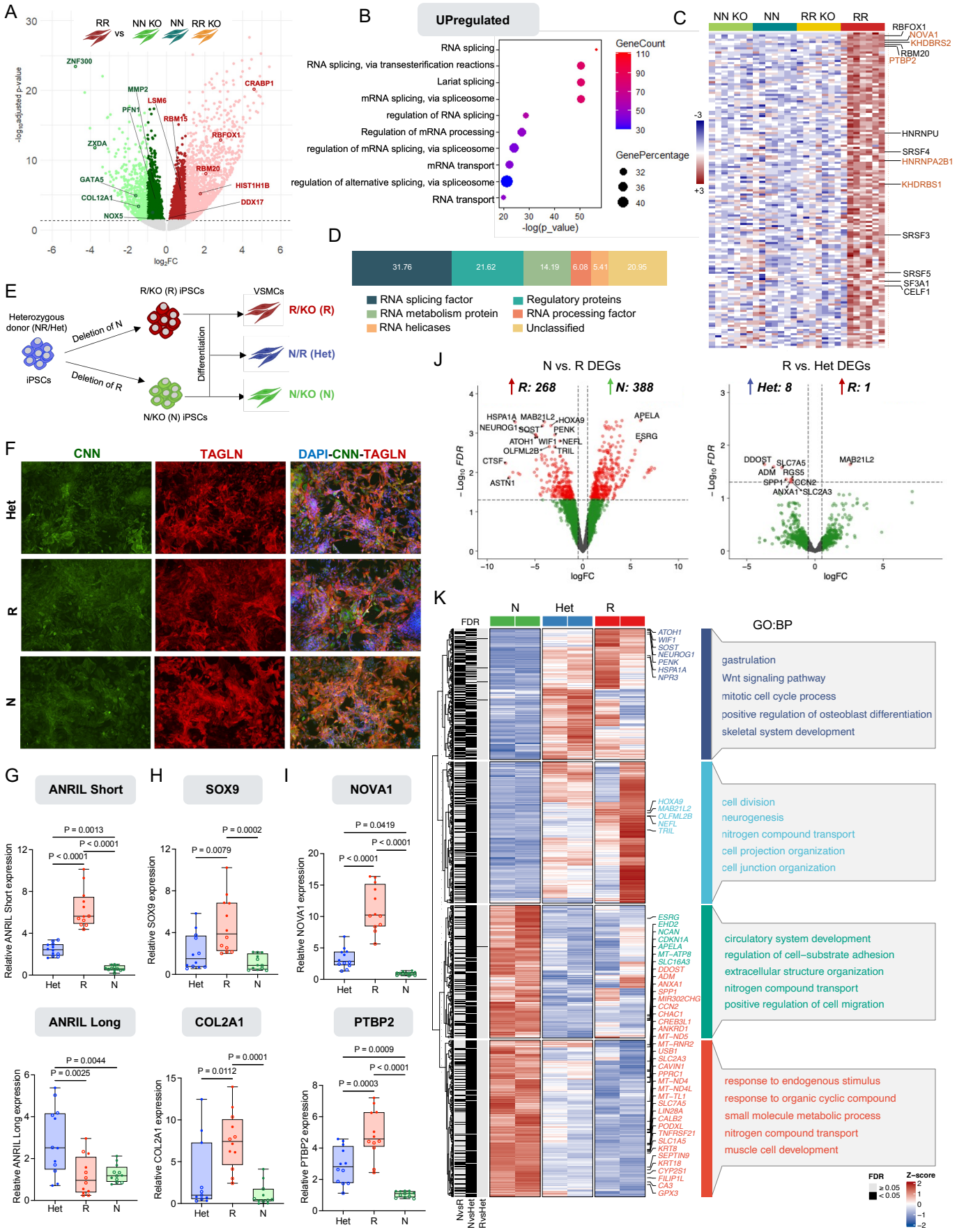
A
RR vs NN KO
NN vs RR KO
ZNF300
MMP2
LSM6
PFN1
RBM15
CRABP1
RBFOX1
ZXDA
RBM20
GATA5
HIST1H1B
COL12A1
DDX17
NOX5
-log10adjusted p-value
log2FC
B
UPregulated
RNA splicing
RNA splicing, via transesterification reactions
Lariat splicing
mRNA splicing, via spliceosome
regulation of RNA splicing
Regulation of mRNA processing
regulation of mRNA splicing, via spliceosome
mRNA transport
regulation of alternative splicing, via spliceosome
RNA transport
-log(p_value)
GeneCount
GenePercentage
C
NN KO
NN
RR KO
RR
RBFOX1
NOVA1
KHDBRS2
RBM20
PTBP2
HNRNPU
SRSF4
HNRNPA2B1
KHDRBS1
SRSF3
SRSF5
SF3A1
CELF1
D
31.76
21.62
14.19
6.08
5.41
20.95
RNA splicing factor
Regulatory proteins
RNA metabolism protein
RNA processing factor
RNA helicases
Unclassified
E
Heterozygous donor (NR/Het)
iPSCs
Deletion of N
Deletion of R
R/KO (R) iPSCs
N/KO (N) iPSCs
Differentiation
VSMCs
R/KO (R)
N/R (Het)
N/KO (N)
F
CNN
TAGLN
DAPI-CNN-TAGLN
Het
R
N
G
ANRIL Short
Relative ANRIL Short expression
P = 0.0013
P < 0.0001
P < 0.0001
ANRIL Long
Relative ANRIL Long expression
P = 0.0044
P = 0.0025
H
SOX9
Relative SOX9 expression
P = 0.0002
P = 0.0079
COL2A1
Relative COL2A1 expression
P = 0.0001
P = 0.0112
I
NOVA1
Relative NOVA1 expression
P = 0.0419
P < 0.0001
P < 0.0001
PTBP2
Relative PTBP2 expression
P = 0.0009
P < 0.0001
P = 0.0003
Het
R
N
J
N vs. R DEGs
R: 268
N: 388
HSPA1A
MAB21L2
HOXA9
NEUROG1
SOST
PENK
APELA
ESRG
ATOH1
WIF1
NEFL
OLFML2B
TRIL
CTSF
ASTN1
logFC
R vs. Het DEGs
Het: 8
R: 1
DDOST
SLC7A5
ADM
RGS5
MAB21L2
SPP1
CCN2
ANXA1
SLC2A3
K
FDR
N
Het
R
ATOH1
WIF1
SOST
NEUROG1
PENK
HSPA1A
NPR3
HOXA9
MAB21L2
OLFML2B
NEFL
TRIL
ESRG
EHD2
NCAN
CDKN1A
APELA
MT-ATP8
SLC16A3
DDOST
ADM
ANXA1
SPP1
MIR302CHG
CCN2
CHAC1
CREB3L1
ANKRD1
MT-ND5
MT-RNR2
USB1
SLC2A3
CAVIN1
PPRC1
MT-ND4
MT-ND4L
MT-TL1
SLC7A5
LIN28A
CALB2
PODXL
TNFRSF21
SLC1A5
KRT8
SEPTIN9
KRT18
CYP2S1
FILIP1L
CA3
GPX3
NvsR
NvsHet
RvsHet
GO:BP
gastrulation
Wnt signaling pathway
mitotic cell cycle process
positive regulation of osteoblast differentiation
skeletal system development
cell division
neurogenesis
nitrogen compound transport
cell projection organization
cell junction organization
circulatory system development
regulation of cell–substrate adhesion
extracellular structure organization
nitrogen compound transport
positive regulation of cell migration
response to endogenous stimulus
response to organic cyclic compound
small molecule metabolic process
nitrogen compound transport
muscle cell development
FDR
≥ 0.05
< 0.05
Z-score

Figure 1

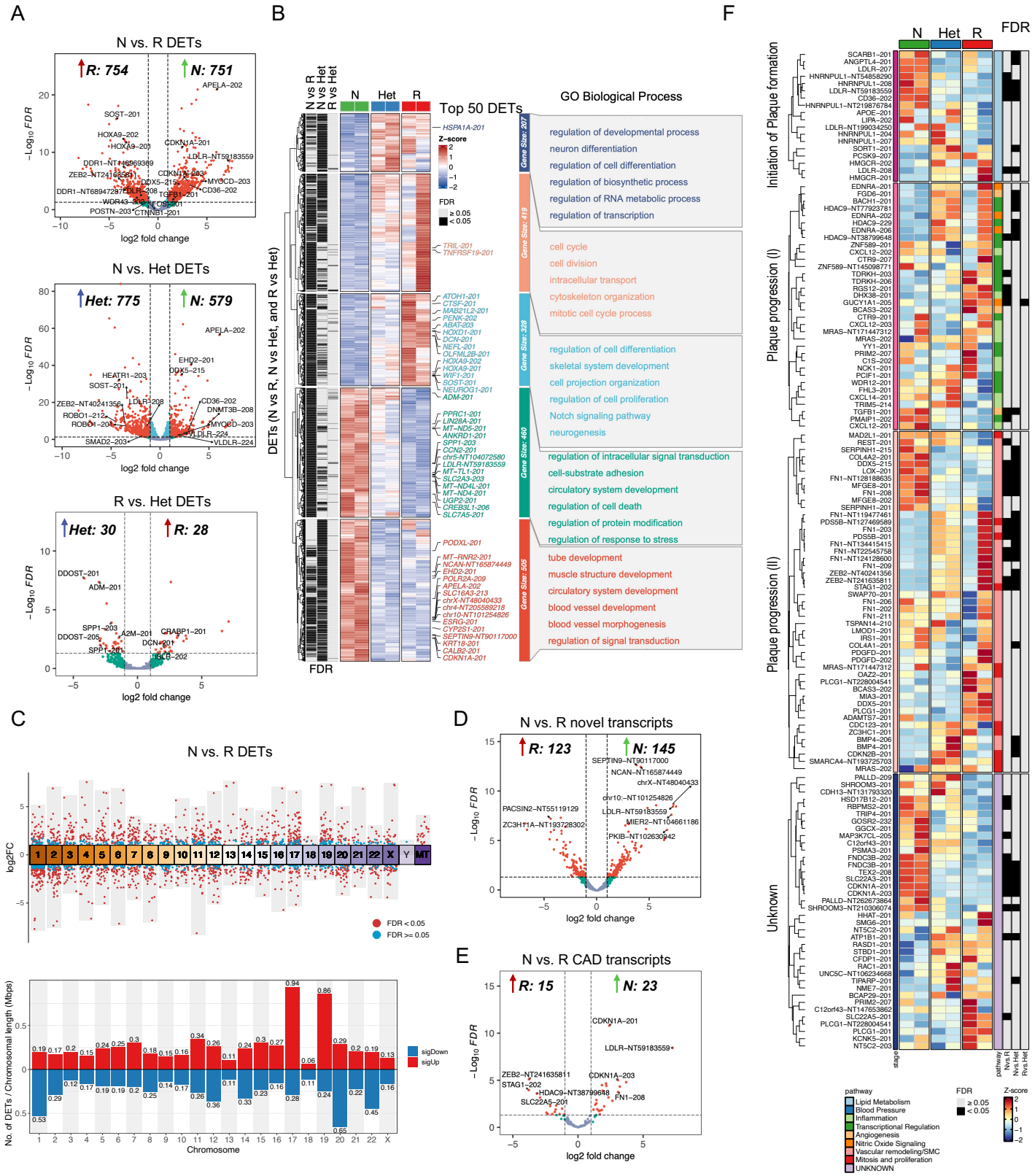
A
N vs. R DETs
R: 754
N: 751
N vs. Het DETs
Het: 775
N: 579
R vs. Het DETs
Het: 30
R: 28
log2 fold change
B
Top 50 DETs
GO Biological Process
DETs (N vs R, N vs Het, and R vs Het)
N
Het
R
FDR
regulation of developmental process
neuron differentiation
regulation of cell differentiation
regulation of biosynthetic process
regulation of RNA metabolic process
regulation of transcription
cell cycle
cell division
intracellular transport
cytoskeleton organization
mitotic cell cycle process
regulation of cell differentiation
skeletal system development
cell projection organization
regulation of cell proliferation
Notch signaling pathway
neurogenesis
regulation of intracellular signal transduction
cell-substrate adhesion
circulatory system development
regulation of cell death
regulation of protein modification
regulation of response to stress
tube development
muscle structure development
circulatory system development
blood vessel development
blood vessel morphogenesis
regulation of signal transduction
C
N vs. R DETs
log2FC
FDR < 0.05
FDR >= 0.05
No. of DETs / Chromosomal length (Mbps)
Chromosome
sigDown
sigUp
D
N vs. R novel transcripts
R: 123
N: 145
log2 fold change
E
N vs. R CAD transcripts
R: 15
N: 23
log2 fold change
F
N
Het
R
FDR
Initiation of Plaque formation
Plaque progression (I)
Plaque progression (II)
Unknown
stage
pathway
Nvs.R
Nvs.Het
Rvs.Het
Lipid Metabolism
Blood Pressure
Inflammation
Transcriptional Regulation
Angiogenesis
Nitric Oxide Signaling
Vascular remodeling/SMC
Mitosis and proliferation
UNKNOWN
Z-score

Figure 2

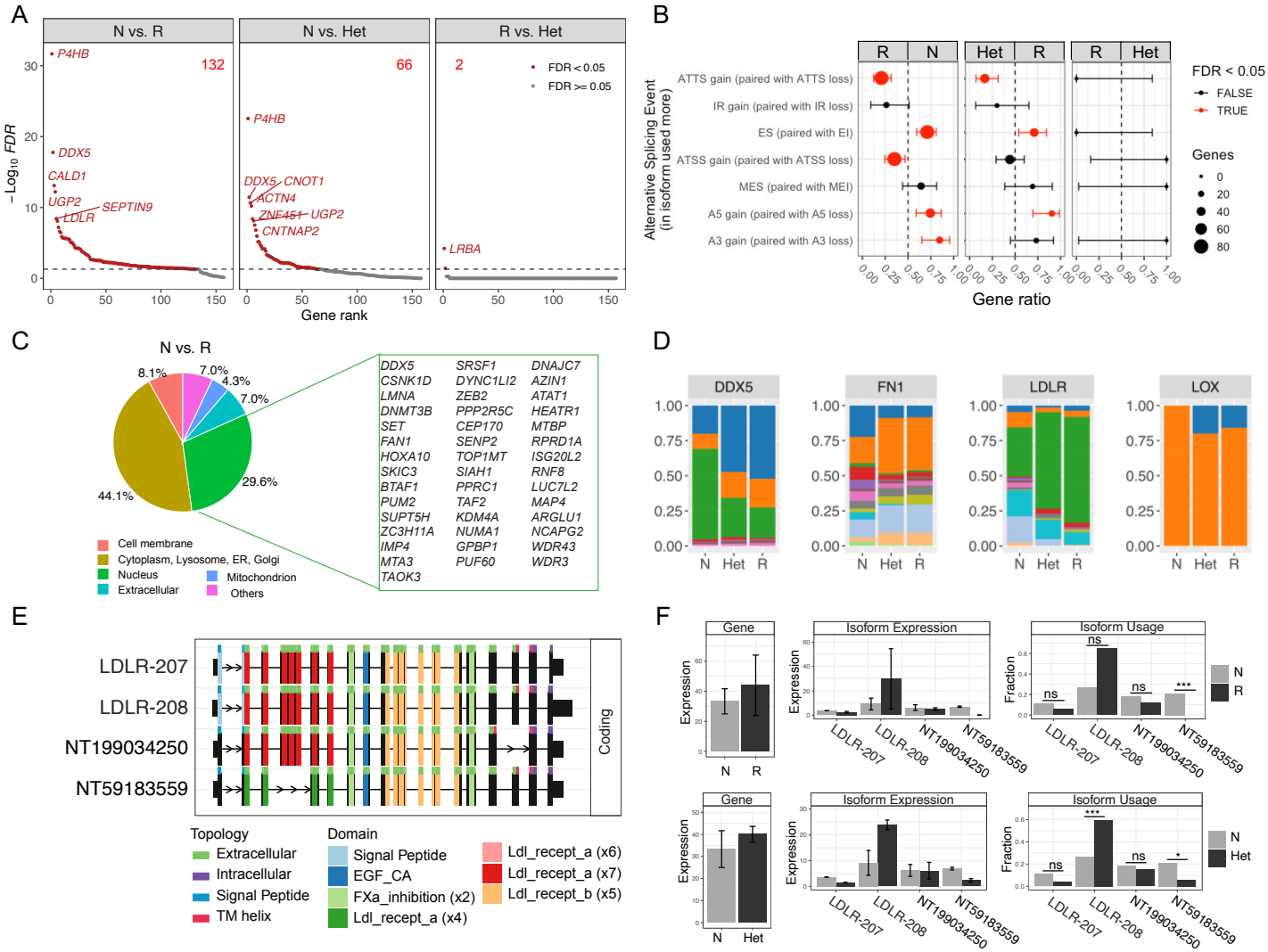
A
N vs. R
N vs. Het
R vs. Het
132
66
2
FDR < 0.05
FDR >= 0.05
P4HB
DDX5
CALD1
UGP2
LDLR
SEPTIN9
CNOT1
ACTN4
ZNF451
CNTNAP2
LRBA
– Log10 FDR
Gene rank
B
Alternative Splicing Event (in isoform used more)
ATTS gain (paired with ATTS loss)
IR gain (paired with IR loss)
ES (paired with EI)
ATSS gain (paired with ATSS loss)
MES (paired with MEI)
A5 gain (paired with A5 loss)
A3 gain (paired with A3 loss)
Gene ratio
FDR < 0.05
FALSE
TRUE
Genes
C
N vs. R
8.1%
7.0%
4.3%
7.0%
29.6%
44.1%
Cell membrane
Cytoplasm, Lysosome, ER, Golgi
Nucleus
Extracellular
Mitochondrion
Others
DDX5 SRSF1 DNAJC7
CSNK1D DYNC1LI2 AZIN1
LMNA ZEB2 ATAT1
DNMT3B PPP2R5C HEATR1
SET CEP170 MTBP
FAN1 SENP2 RPRD1A
HOXA10 TOP1MT ISG20L2
SKIC3 SIAH1 RNF8
BTAF1 PPRC1 LUC7L2
PUM2 TAF2 MAP4
SUPT5H KDM4A ARGLU1
ZC3H11A NUMA1 NCAPG2
IMP4 GPBP1 WDR43
MTA3 PUF60 WDR3
TAOK3
D
DDX5
FN1
LDLR
LOX
N Het R
E
LDLR-207
LDLR-208
NT199034250
NT59183559
Coding
Topology
Extracellular
Intracellular
Signal Peptide
TM helix
Domain
Signal Peptide
EGF_CA
FXa_inhibition (x2)
Ldl_recept_a (x4)
Ldl_recept_a (x6)
Ldl_recept_a (x7)
Ldl_recept_b (x5)
F
Gene
Isoform Expression
Isoform Usage
Expression
Fraction
N R
N Het
ns
***
*
LDLR-207
LDLR-208
NT199034250
NT59183559

Figure 3

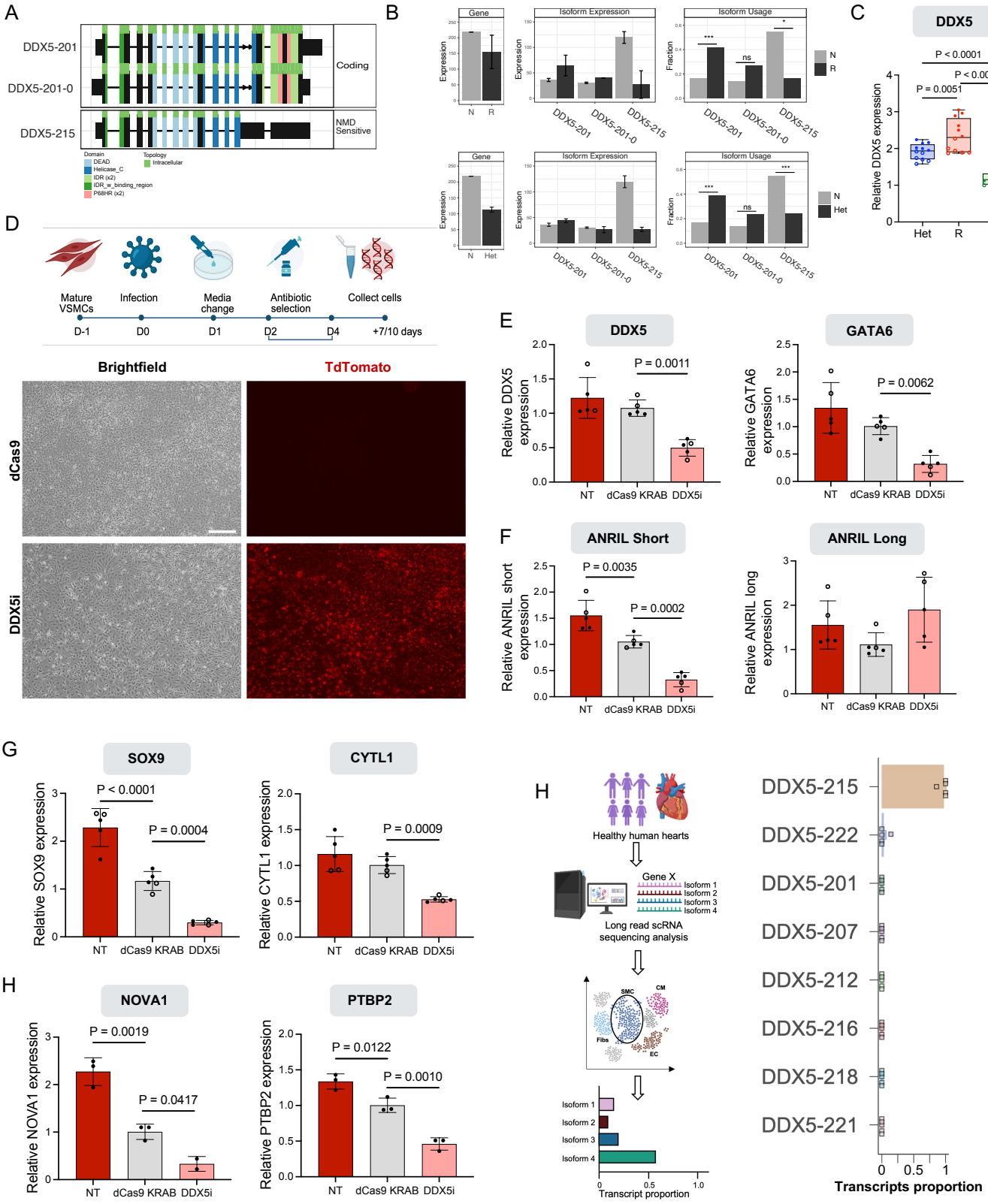
A
DDX5-201
DDX5-201-0
DDX5-215
Coding
NMD Sensitive
Domain
DEAD
Helicase_C
IDR (x2)
IDR_w_binding_region
P68HR (x2)
Topology
Intracellular
B
Gene
Isoform Expression
Isoform Usage
Expression
Fraction
N
R
Het
DDX5-201
DDX5-201-0
DDX5-215
ns
C
DDX5
P < 0.0001
P = 0.0051
Relative DDX5 expression
Het
R
N
D
Mature VSMCs
Infection
Media change
Antibiotic selection
Collect cells
D-1
D0
D1
D2
D4
+7/10 days
Brightfield
TdTomato
dCas9
DDX5i
E
DDX5
P = 0.0011
Relative DDX5 expression
GATA6
P = 0.0062
Relative GATA6 expression
NT
dCas9 KRAB
DDX5i
F
ANRIL Short
P = 0.0035
P = 0.0002
Relative ANRIL short expression
ANRIL Long
Relative ANRIL long expression
G
SOX9
P < 0.0001
P = 0.0004
Relative SOX9 expression
CYTL1
P = 0.0009
Relative CYTL1 expression
H
NOVA1
P = 0.0019
P = 0.0417
Relative NOVA1 expression
PTBP2
P = 0.0122
P = 0.0010
Relative PTBP2 expression
H
Healthy human hearts
Gene X
Isoform 1
Isoform 2
Isoform 3
Isoform 4
Long read scRNA sequencing analysis
SMC
CM
Fibs
EC
Transcript proportion
DDX5-215
DDX5-222
DDX5-201
DDX5-207
DDX5-212
DDX5-216
DDX5-218
DDX5-221
Transcripts proportion

Figure 4

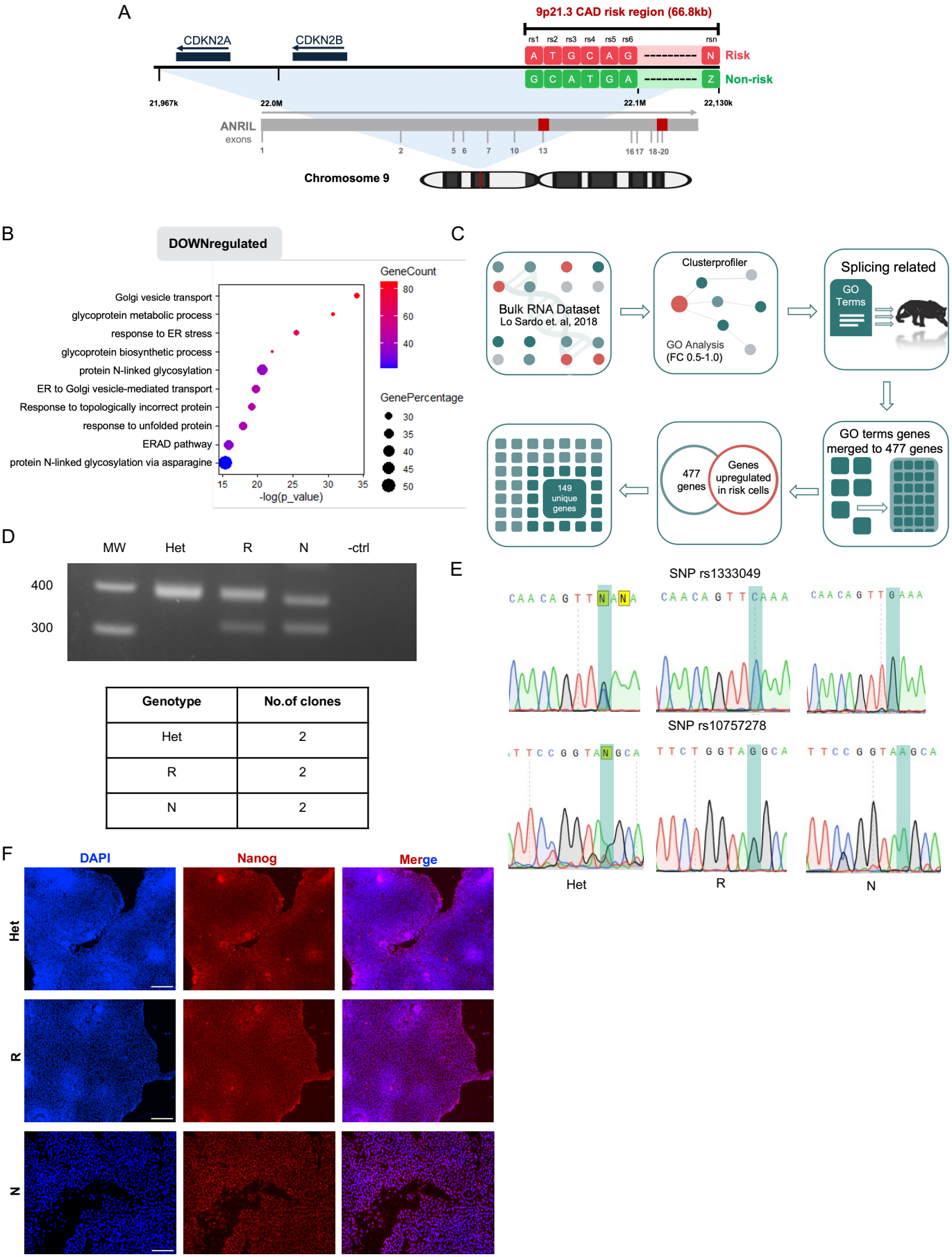

Genotype	No.of clones
Het	2
R	2
N	2

Figure S1

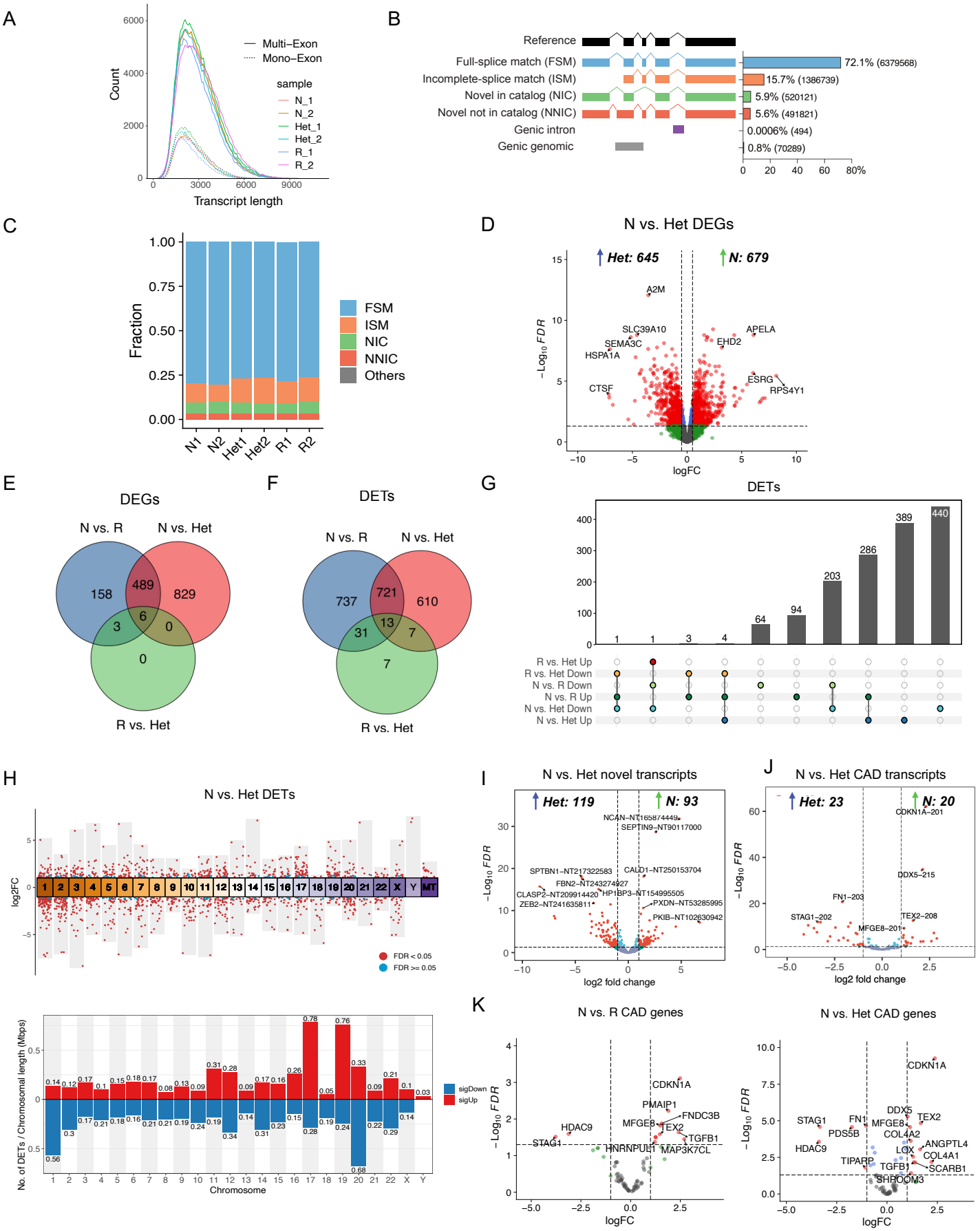
A
Count
Transcript length
Multi−Exon
Mono−Exon
sample
N_1
N_2
Het_1
Het_2
R_1
R_2
B
Reference
Full-splice match (FSM)
Incomplete-splice match (ISM)
Novel in catalog (NIC)
Novel not in catalog (NNIC)
Genic intron
Genic genomic
72.1% (6379568)
15.7% (1386739)
5.9% (520121)
5.6% (491821)
0.0006% (494)
0.8% (70289)
C
Fraction
FSM
ISM
NIC
NNIC
Others
N1
N2
Het1
Het2
R1
R2
D
N vs. Het DEGs
Het: 645
N: 679
logFC
E
DEGs
N vs. R
N vs. Het
R vs. Het
F
DETs
G
DETs
R vs. Het Up
R vs. Het Down
N vs. R Down
N vs. R Up
N vs. Het Down
N vs. Het Up
H
N vs. Het DETs
log2FC
FDR < 0.05
FDR >= 0.05
No. of DETs / Chromosomal length (Mbps)
Chromosome
sigDown
sigUp
I
N vs. Het novel transcripts
Het: 119
N: 93
log2 fold change
J
N vs. Het CAD transcripts
Het: 23
N: 20
log2 fold change
K
N vs. R CAD genes
N vs. Het CAD genes
logFC

Figure S2

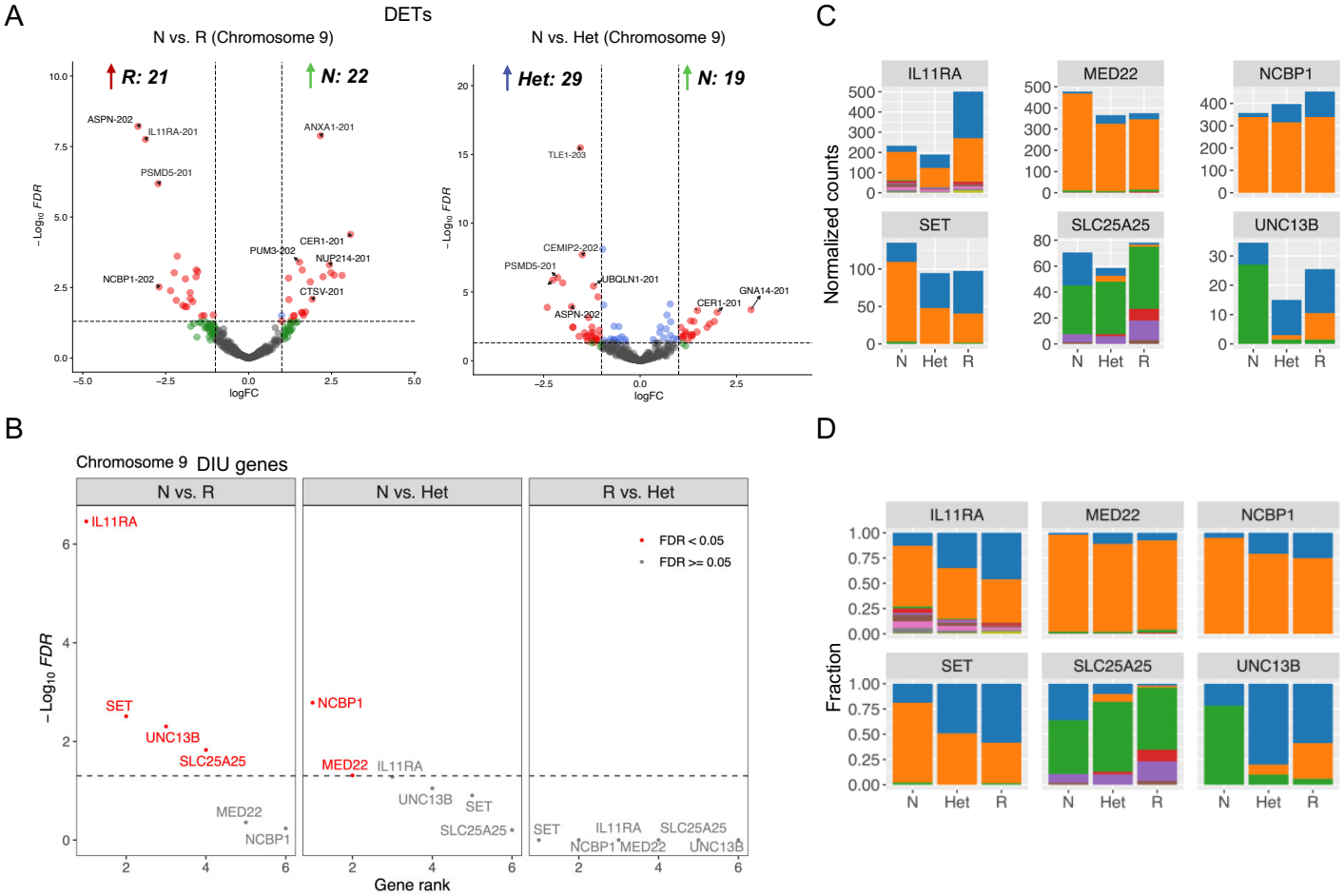
A
DETs
N vs. R (Chromosome 9)
R: 21
N: 22
ASPN-202
IL11RA-201
PSMD5-201
NCBP1-202
ANXA1-201
PUM3-202
CER1-201
NUP214-201
CTSV-201
−Log10 FDR
logFC
N vs. Het (Chromosome 9)
Het: 29
N: 19
TLE1-203
CEMIP2-202
PSMD5-201
UBQLN1-201
ASPN-202
CER1-201
GNA14-201
C
IL11RA
MED22
NCBP1
SET
SLC25A25
UNC13B
Normalized counts
N
Het
R
B
Chromosome 9 DIU genes
N vs. R
N vs. Het
R vs. Het
FDR < 0.05
FDR >= 0.05
IL11RA
SET
UNC13B
SLC25A25
MED22
NCBP1
Gene rank
D
Fraction

Figure S3

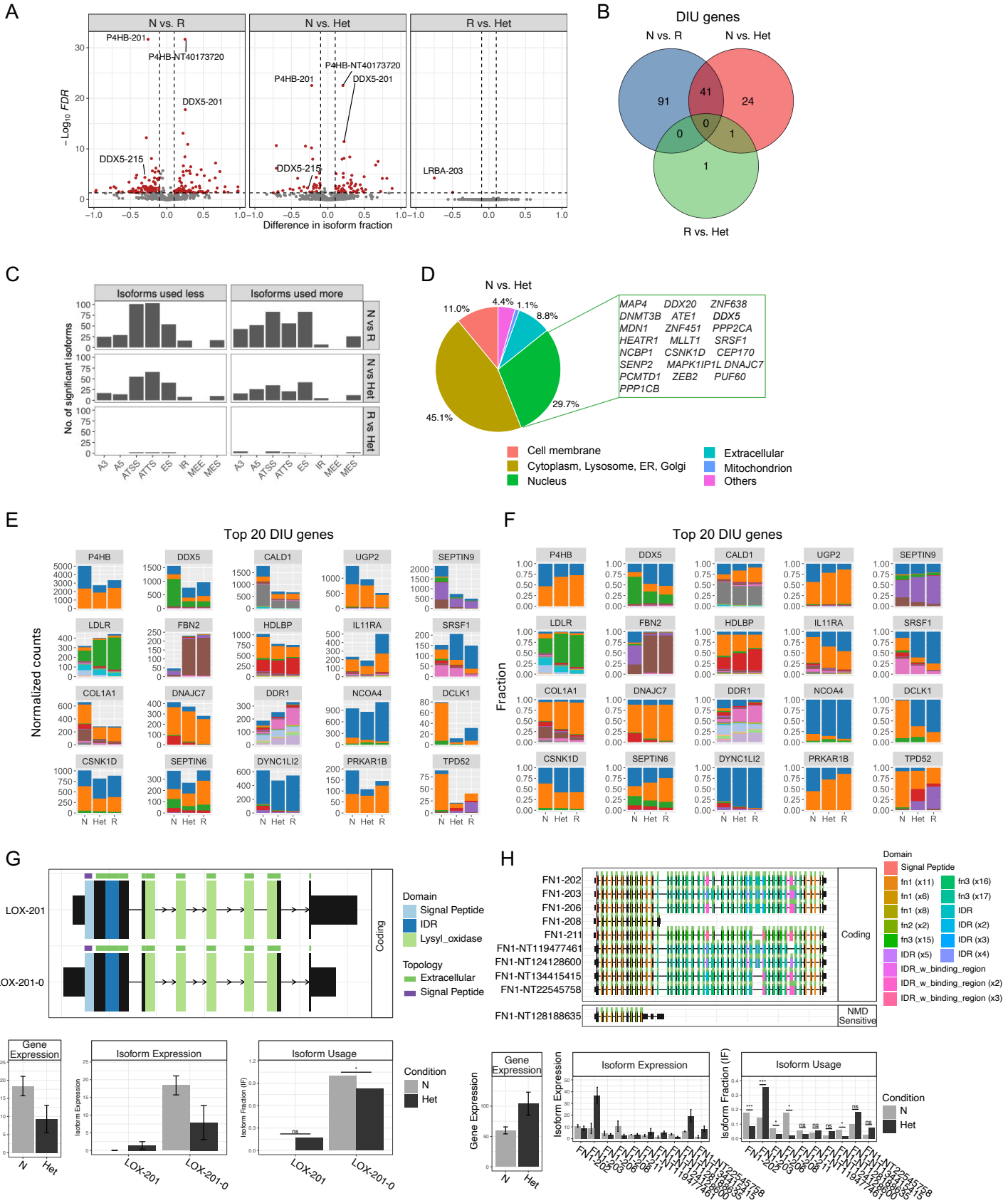
A
N vs. R
N vs. Het
R vs. Het
P4HB-201
P4HB-NT40173720
DDX5-201
DDX5-215
LRBA-203
– Log10 FDR
Difference in isoform fraction
B
DIU genes
N vs. R
N vs. Het
R vs. Het
91
41
24
0
0
1
1
C
Isoforms used less
Isoforms used more
N vs R
N vs Het
R vs Het
No. of significant isoforms
A3
A5
ATSS
ATTS
ES
IR
MEE
MES
D
N vs. Het
11.0%
4.4%
1.1%
8.8%
29.7%
45.1%
MAP4 DDX20 ZNF638
DNMT3B ATE1 DDX5
MDN1 ZNF451 PPP2CA
HEATR1 MLLT1 SRSF1
NCBP1 CSNK1D CEP170
SENP2 MAPK1IP1L DNAJC7
PCMTD1 ZEB2 PUF60
PPP1CB
Cell membrane
Cytoplasm, Lysosome, ER, Golgi
Nucleus
Extracellular
Mitochondrion
Others
E
Top 20 DIU genes
Normalized counts
P4HB
DDX5
CALD1
UGP2
SEPTIN9
LDLR
FBN2
HDLBP
IL11RA
SRSF1
COL1A1
DNAJC7
DDR1
NCOA4
DCLK1
CSNK1D
SEPTIN6
DYNC1LI2
PRKAR1B
TPD52
N Het R
F
Top 20 DIU genes
Fraction
G
LOX-201
LOX-201-0
Coding
Domain
Signal Peptide
IDR
Lysyl_oxidase
Topology
Extracellular
Signal Peptide
Gene Expression
Isoform Expression
Isoform Usage
Isoform Fraction (IF)
Condition
N
Het
H
FN1-202
FN1-203
FN1-206
FN1-208
FN1-211
FN1-NT119477461
FN1-NT124128600
FN1-NT134415415
FN1-NT22545758
FN1-NT128188635
Coding
NMD Sensitive
Domain
Signal Peptide
fn1 (x11)
fn1 (x6)
fn1 (x8)
fn2 (x2)
fn3 (x15)
IDR (x5)
fn3 (x16)
fn3 (x17)
IDR
IDR (x2)
IDR (x3)
IDR (x4)
IDR_w_binding_region
IDR_w_binding_region (x2)
IDR_w_binding_region (x3)
Gene Expression
Isoform Expression
Isoform Fraction (IF)
Isoform Usage
Condition
N
Het

Figure S4

A

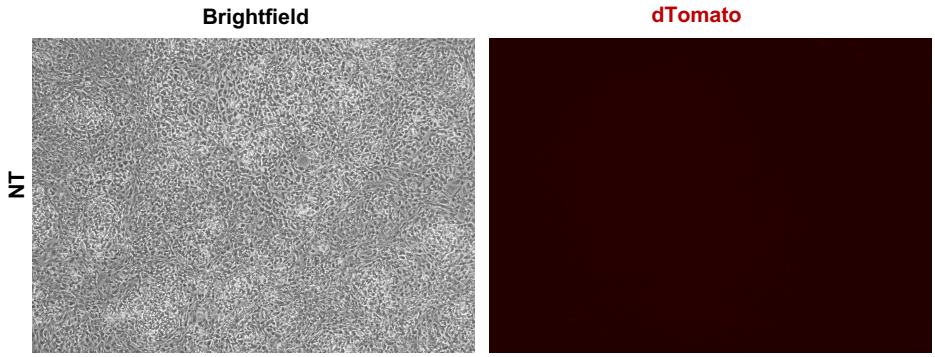

B

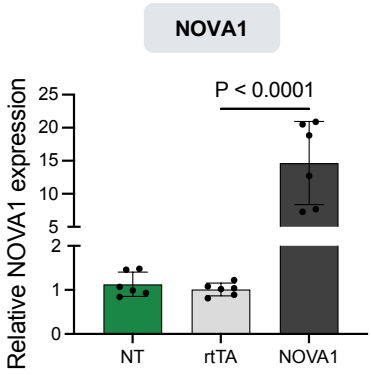

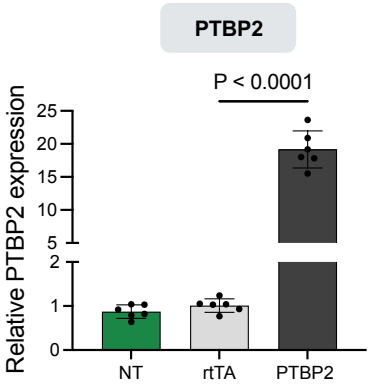

C

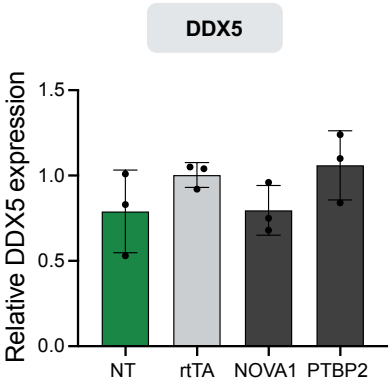

Figure S5

Figure Legends

Figure 1. The 9p21.3 CAD risk locus impacts splicing processes. (A) Volcano plot of differentially expressed genes from bulk RNA sequencing performed on iPSC-derived VSMCs homozygous risk for the 9p21.3 locus (RR) compared to homozygous non-risk cells (NN) and isogenic VSMCs deleted of the 9p21.3 locus in both backgrounds (RRKO, NNKO) (Lo Sardo et.al, 2018). Light red and green are the genes analyzed in Lo Sardo et al. (2018). Red and green colored genes were analyzed in this study from absolute $\log_2$ fold change 0.1-1.0. **(B)** The top 10 gene ontology terms enriched in the differentially expressed genes in RR VSMCs between $\log_2$ fold change 0.1-1.0. **(C)** Heatmap of the top 149 differentially expressed splicing genes in iPSC-VSMCs across four genotypes at 9p21.3. N=7 per genotype. **(D)** Bar chart showing the biological function classification of the 149 splicing-related genes. **(E)** Schematic of experimental workflow for the generation of a new collection of isogenic iPSC. iPSCs are from one heterozygous donor (N/R- Het). Isogenic knockout lines were derived by TALEN-mediated haplotype editing to delete the entire CAD region and generate hemizygous lines (R/KO-R, N/KO-R). Cells were differentiated to VSMCs and used for long-read PacBio sequencing. **(F)** Immunocytochemistry for VSMCs markers for Het, R, and N VSMCs. Scale is 100 μm. **(G-I)** qPCR quantification of ANRIL short and long isoforms **(G)**, Osteochondrogenic markers SOX9 and COL2A1**(H)**, and the splicing genes NOVA1 and PTBP2 (**I**). Data are from 2 independent cell lines per genotype and three independent VSMCs differentiation experiments. P-value calculated with One-way ANOVA with Bonferroni correction. **(J)** Volcano plots illustrate genome-wide differential gene expression between Non-risk (N) vs. Risk (R), and Risk vs. Heterozygous (Het) comparisons. logFC: log2 fold change. **(K)** Heatmap and Gene Ontology (GO) enrichment between N, Het, and R genotypes for DEGs.

Figure 2. Haplotype-biased transcript isoforms expression controls cell fate in VSMCs. (A) Volcano plots illustrate genome-wide differential transcript expression between Non-risk (N) vs. Risk (R), Non-risk vs. Heterozygous (Het), and Risk vs. Heterozygous comparisons. **(B)** Heatmap and Gene Ontology (GO) enrichment between N, R, and Het genotypes for DETs upregulated and downregulated. **(C)** Chromosomal distribution of DETs with $\log_2$ fold changes across the genome for N vs R haplotypes. Each dot represents a transcript positioned along chromosomes 1–22, X, and Y, as well as mitochondrial DNA. Bar plots showing the number of DETs per chromosome normalized to chromosome length for N vs R. Red bars indicate upregulated DETs, blue bars indicate downregulated DETs. **(D)** Volcano plots showing differential expression of novel transcripts (NIC and NNIC)**,** for N vs R VSMCs. **(E)** Volcano plots showing differential expression of CAD-associated transcripts**,** for N vs R VSMCs. **(F)** Heatmap enrichment between N, R, and Het genotypes for DETs related to genes associated to CAD progression according to Kesseler et.al, 2019.

Figure 3. The risk haplotype at 9p21.3 drives divergent transcript isoform usage in VSMCs. (A) Ranked gene plots showing differential isoform usage between Non-risk (N), Risk (R), and Heterozygous (Het) groups. Red dots indicate genes with significant changes (FDR < 0.05). **(B)** Alternative

splicing event types associated with isoforms used more across comparisons. Each dot represents a splicing event category, with dot size indicating the number of affected genes. Significant events (FDR < 0.05) are shown in red. **(C)** Pie charts indicate the cellular localization of proteins encoded by genes undergoing significant isoform switching between N vs. R haplotypes. **(D)** Stacked bar charts illustrating isoform usage proportions of key CAD-related genes (DDX5, FN1, LDLR, LOX) across N, Het, and R genotypes. Each color represents a distinct transcript isoform. **(E)** Schematic representation showing distinct exon composition and domain architecture of LDLR protein isoforms. **(F)** Bar graphs show gene-level expression, isoform-specific expression, and isoform usage of LDLR transcripts between N vs. R, and N vs. Het.

Figure 4. DDX5 targeting ameliorate the effect of the 9p21.3 risk haplotype in VSMCs. (A) Schematic representation showing distinct exon composition and domain architecture of DDX5 protein isoforms. **(B)** Bar graphs show gene-level expression, isoform-specific expression, and isoform usage of DDX5 transcripts between N vs. R, and N vs. Het. **(C)** qPCR quantification of DDX5 isoform using isoform-specific primers. Data are from 2 independent cell lines per genotype and three independent differentiation experiments. **(D)** Schematic of CRISPR interference (CRISPRi) timeline in mature Risk VSMCs**.** Representative brightfield and fluorescence images of VSMCs upon CRISPRi with dCas9-KRAB only (control) and DDX5i- TdTomato (transduced with dCas9-KRAB and DDX5-specific gRNA with TdTomato reporter). Scale is 200 μm. **(E-F)** qPCR quantification of DDX5, and GATA6 **(E)** and ANRIL isoforms **(F)**. **(G-H)** qPCR quantification of osteochondrogenic markers **(G)**, and splicing genes **(H)**. Data are from two independent experiments. P-value calculated with One-way ANOVA with Bonferroni correction. **(I)** Detection of DDX5 transcripts(reference-based) in the Heart Isoform Atlas (https://gaolabtools.shinyapps.io/heart-isoform-atlas/) from Pan et al 2025. The quantification relates to the smooth muscle cell population in non-disease heart samples.

Figure S1. Evaluation of splicing genes alteration and validation of the new isogenic iPSC collection. (A) Schematic of the 9p21.3 coronary artery disease locus. The cartoon shows the human chromosome 9 and the 66.8 Kb CAD risk region. The CAD locus is flanked by the CDKN2A and B genes and overlaps with the ANRIL gene. Red square in the ANRIL gene indicate the two sites for termination of transcription in exon 13 and 20. Within the CAD region a simplified schematic of the different pattern of SNPs (rs) at the region resulting in two possible alleles (risk and non-risk). **(B)** The top 10 gene ontology terms downregulated in the differentially expressed genes in RR VSMCs between $\log_2$ fold change 0.1-1.0. **(C)** Schematic of workflow to prioritize genes related to splicing**. (D)** R, N, and Het iPSCs were genotyped for the deletion by PCR as we previously described (Lo Sardo et al 2018). 2 clones per genotype were generated and used for experiments. **(E)** The genotype of the newly generated iPSCs was confirmed by Sanger sequencing for two SNPs at the 9p21.3 CAD locus (rs1333049, rs10757278). **(F)** Immunocytochemistry for the pluripotency marker Nanog for Het, R, and N iPSCs. Scale is 100 μm.

Figure S2. Pac-Bio long read sequencing of VSMCs with different haplotypes at the 9p21.3 CAD locus. (A) Distribution of transcript lengths across samples, showing multi-exon (solid lines) and exon (dashed lines) transcripts. **(B)** Classification of transcripts based on splice junction matching to known annotations, including full-splice match (FSM), incomplete-splice match (ISM), novel isoforms in catalog (NIC), and novel not in catalog (NNIC), along with genic and intergenic categories. Percentages represent the proportion of each class. **(C)** Fraction of isoform types in each sample, demonstrating the relative abundance of FSM, ISM, NIC, NNIC, and other categories across all biological replicates. **(D)** Volcano plots illustrate genome-wide differential gene expression between N vs. Het VSMCs. logFC: log2 fold change. **(E)** Venn diagram representing the overlap of DEGs (FDR < 0.05 and log_2FC > 1 or <-1) across the three genotypes. **(F)** Venn diagram representing the overlap of DETs (FDR < 0.05 and log_2FC > 1 or <-1) across the three genotypes. **(G)** Upset plot represents the intersection structure of DETs. Bars represent the size of DET subsets, while the connected dots below each bar indicate which comparisons contribute to each subset. **(H)** Chromosomal distribution of DETs for log_2 fold changes across the genome for N vs. Het haplotypes. Each dot represents a transcript positioned along chromosomes 1–22, X, and Y, as well as mitochondrial DNA. Bar plots showing the number of DETs per chromosome normalized to chromosome length, for N vs Het. Red bars indicate upregulated DETs, blue bars indicate downregulated DETs. **(I)** Volcano plots showing differential expression of novel transcripts (NIC and NNIC)**,** for N vs Het VSMCs. **(J)** Volcano plots showing differential expression of CAD-associated transcripts**,** for N vs Het VSMCs. **(K)** Volcano plots showing differential expression of CAD-associated genes**,** for N vs R VSMCs and N vs Het.

Figure S3. Differential transcripts analysis at chromosome 9 (A) Volcano plots illustrate the differential expression of transcripts in chromosome 9. **(B)** Genes showing differential isoform usage (DIU) are ranked based on the -log10 FDR of DIU. **(C-D)** The DIU of significant isoform switch genes is presented using normalized counts **(C)** and fraction **(D)**. Each color represents a distinct transcript isoform.

Figure S4. Differential transcript usage driven by different haplotypes at 9p21.3. (A) Volcano plots showing differential isoform usage between Non-risk (N), Risk (R), and Heterozygous (Het) groups. Red dots indicate isoforms with significant changes (FDR < 0.05). **(B)** Venn diagram representing the overlap of DTUs across the three genotypes. **(C)** Bar charts showing the distribution of alternative splicing event types among isoforms used less **(left)** and more **(right)** in each genotype comparison. **(D)** Pie charts representing the distribution of cellular localization of proteins encoded by genes undergoing significant isoform switching between N vs. Het haplotypes. **(E-F)** DIU of the top 20 genes by normalized counts **(E)** and fractions **(F)** between genotypes. Each color represents a distinct transcript isoform. **(G)** Schematic representation showing distinct exon composition and domain architecture of LOX protein isoforms. Bar graphs demonstrate gene-level expression, isoform-specific expression, and isoform usage of LOX between N vs. Het. **(F)** Schematic representation showing distinct exon composition and domain

architecture of FN1 protein isoforms. Bar graphs demonstrate gene-level expression, isoform-specific expression, and isoform usage of FN1 between N vs. Het.

Figure S5. DDX5 expression is independent of splicing genes. (A) Representative brightfield and fluorescence images of VSMCs from the DDX5i experiments with no viral infection (NT) relative to Figure 4D. Scale is 200 μm. **(B)** qPCR quantification of overexpression of splicing genes NOVA1 and PTBP2 **(C)** qPCR quantification of DDX5 in cells overexpressing the splicing genes NOVA1 and PTBP2. P-value calculated with One-way ANOVA with Bonferroni correction.

Table S1: Gene ontology terms upregulated in 9p21 RR cells related to Fig.1B
Table S2: Gene ontology terms downregulated in 9p21 RR cells related to Fig.S1A
Table S3: List of splicing genes upregulated in RR cells related to Fig.1C
Table S4: DEGs between N vs R VSMCs related to Fig.1J
Table S5: DEGS between N vs Het VSMCs related to Fig.S1D
Table S6: DEGs between R vs Het VSMCs related to Fig.1J
Table S7: DETs between N vs R VSMCs related to Fig.2A
Table S8: DETs between N vs Het VSMCs related to Fig.2A
Table S9: DETs between R vs Het VSMCs related to Fig.2A
Table S10: All DETs between the N, R, and Het VSMCs related to Fig.2B and 2F
Table S11: List of all novel transcripts between N, R and Het VSMCs related to Fig.2D and Fig.S2I
Table S12: List of all CAD transcripts between N, R and Het VSMCs related to Fig.2E and Fig.S2J
Table S13: All DTUs between N vs R related to Fig.3A
Table S14: All DTUs between N vs Het related to Fig.3A